

2

The FDTD Method: Essences, Evolutions, and Applications to Nano-Optics and Quantum Physics

Xiaoyan Y.Z. Xiong and Wei E.I. Sha

*Department of Electrical and Electronic Engineering,
University of Hong Kong, Hong Kong, China*

CONTENTS

2.1	Introduction.....	38
2.1.1	Discretization Strategies in the Time Domain	39
2.1.1.1	Runge-Kutta Method.....	40
2.1.1.2	Second-Order Leap-Frog (Staggered) Time- Stepping Approach	40
2.1.1.3	Unconditionally Stable Algorithms.....	41
2.1.1.4	High-Order Symplectic Integration Scheme.....	42
2.1.2	Space Discretization Methods	42
2.1.2.1	Second-Order Leap-Frog (Staggered) Difference	42
2.1.2.2	Fourth-Order Staggered Difference	42
2.1.2.3	Fourth-Order Implicit Compact Difference Algorithm.....	43
2.1.2.4	Multiresolution Expansion Method	43
2.1.2.5	Pseudo-Spectral Scheme	43
2.2	Core Techniques.....	44
2.2.1	Basic Update Equations and Material Averaging Technique....	45
2.2.2	Absorbing Boundary Condition.....	47
2.2.3	Source Excitations.....	48
2.2.4	Near-to-Far-Field Transformation	51
2.2.5	Periodic Structures	51
2.2.6	Dispersive Media	53
2.3	Numerical Examples for Nano-Optics Applications.....	54
2.3.1	Thin-Film Solar Cells	55
2.3.2	Nanoantennas	59
2.3.3	Spontaneous Emissions	61
2.3.4	Metamaterials.....	62

2.4	Extended to a Time-Dependent Schrödinger Equation	65
2.5	Numerical Examples for Quantum Physics.....	71
2.5.1	1D Propagation Problem.....	71
2.5.2	Two-Dimensional Eigenvalue Problem	72
2.6	Conclusion	74
	Acknowledgment.....	75
	References.....	75

2.1 Introduction

This chapter aims to introduce the recent developments, basic theories, core techniques, real-world applications, and future directions for the finite-difference time-domain (FDTD) method. The unified theoretical frameworks of the FDTD method and its advances (Runge Kutta-FDTD, symplectic FDTD, alternative direction implicit-FDTD, high-order FDTD, multiresolution-TD, pseudospectral-TD, etc.) for solving Maxwell's equations are systematically reviewed in Section 2.1. Next, we will briefly describe core techniques of the FDTD method (involving the basic update equations, material averaging technique, perfectly matched layer, source excitation, near-to-far-field transformation, periodic boundary condition, and treatment of dispersive media) and particularly focus on those for nano-optics applications in Section 2.2. In Section 2.3, we will demonstrate powerful capabilities of the FDTD method to model versatile physical problems in the nano-optics field. The case studies on plasmonic solar cells, nanoantennas, spontaneous emissions, and metamaterials will be discussed with detailed physical understandings. Then, the numerical analyses and implementations of the FDTD method to simulate the Schrödinger equation are presented in Section 2.4. In Section 2.5, we will show several simple examples on the numerical solution of quantum physics problems with the FDTD method. Finally, the conclusion and future direction are summarized in Section 2.6.

The concept of Yee grid was proposed in 1966 [1]. Until now, the traditional finite-difference time-domain (FDTD) method [2–4] has been widely applied to broad-band, transient, and full-wave analyses for solving Maxwell's equations owing to its simplicity, generality, and facility for parallel computing. However, the FDTD method has two main drawbacks. One is the undesirable numerical results caused by the significant accumulated errors from numerical instability, dispersion, and anisotropy, especially for long-term simulations and electrically large objects. Another is the inability to accurately model curved conducting surfaces and material discontinuities by using the staircase model with structured grids.

To overcome the two shortcomings, a variety of improved methods were proposed. Reviews of recent advances in the FDTD method will not only facilitate developing fast and efficient solvers in the computational

electromagnetics field but also gain physical and mathematical insights to solve real-world engineering problems.

Any field components in Maxwell's equations can be defined as

$$F(x, y, z, t) = F^{n+l/m}(i\Delta_x, j\Delta_y, k\Delta_z, (n + \tau_l)\Delta_t) \quad (2.1)$$

where Δ_x , Δ_y , and Δ_z are the space steps respectively along the x -, y -, and z -directions, Δ_t is the time step, i, j, k, n, l , and m are integers, $n+l/m$ denotes the l th stage iteration after n time steps, m is the number of stages in each time step, and $\tau_l\Delta_t$ is the time increment corresponding to the l th stage.

The Maxwell's equations can be written as the following form

$$\frac{\partial}{\partial t} \begin{pmatrix} \mathbf{H} \\ \hat{\mathbf{E}} \end{pmatrix} = L \begin{pmatrix} \mathbf{H} \\ \hat{\mathbf{E}} \end{pmatrix} \quad (2.2)$$

$$L = \begin{pmatrix} \{0\}_{3 \times 3} & -\frac{1}{\sqrt{\mu_0 \epsilon_0}} \mathfrak{R}_{3 \times 3} \\ \frac{1}{\sqrt{\mu_0 \epsilon_0}} \mathfrak{R}_{3 \times 3} & \{0\}_{3 \times 3} \end{pmatrix} \hat{\mathbf{E}} = \sqrt{\frac{\epsilon_0}{\mu_0}} \mathbf{E} \quad (2.3)$$

$$\mathfrak{R} = \begin{pmatrix} 0 & -\frac{\partial}{\partial z} & \frac{\partial}{\partial y} \\ \frac{\partial}{\partial z} & 0 & -\frac{\partial}{\partial x} \\ -\frac{\partial}{\partial y} & \frac{\partial}{\partial x} & 0 \end{pmatrix} = \nabla \times \quad (2.4)$$

where $\mathbf{E} = (E_x, E_y, E_z)^T$ is the electric field, $\mathbf{H} = (H_x, H_y, H_z)^T$ is the magnetic field, T denotes the transpose, $\{0\}_{3 \times 3}$ is the 3×3 null matrix, \mathfrak{R} is the curl operator, and ϵ_0 and μ_0 are the permittivity and permeability of free space.

The analytical solution of (2.2) from $t = 0$ to $t = \Delta_t$ is

$$\begin{pmatrix} \mathbf{H} \\ \hat{\mathbf{E}} \end{pmatrix}(\Delta_t) = \exp(\Delta_t L) \begin{pmatrix} \mathbf{H} \\ \hat{\mathbf{E}} \end{pmatrix}(0) \quad (2.5)$$

2.1.1 Discretization Strategies in the Time Domain

Regarding the time domain, to approximate the time evolution matrix $\exp(\Delta_t L)$, various discretization methods are proposed.

2.1.1.1 Runge-Kutta Method [3, 5, 6]

Using Taylor series to expand the time evolution matrix, we have

$$\exp(\Delta_t L) = I + \Delta_t L + (\Delta_t L)^2 / 2! + (\Delta_t L)^3 / 3! + (\Delta_t L)^4 / 4! + O(\Delta_t^5) \quad (2.6)$$

A multistage strategy can be adopted to approach (2.6). The numerical implementation of the Runge-Kutta (R-K) method from the n th time step to the $(n + 1)$ th time step is given by

$$\mathbf{F}^{n+1} = \mathbf{F}^n + (\Delta_t / 6) \times (\mathbf{F}_1 + 2\mathbf{F}_2 + 2\mathbf{F}_3 + \mathbf{F}_4) \quad (2.7)$$

$$\mathbf{F}_1 = L(t, \mathbf{F}^n), \quad \mathbf{F}_2 = L\left(t + \Delta_t / 2, \mathbf{F}^n + (\Delta_t / 2) \cdot \mathbf{F}_1\right) \quad (2.8)$$

$$\mathbf{F}_3 = L\left(t + \Delta_t / 2, \mathbf{F}^n + (\Delta_t / 2) \cdot \mathbf{F}_2\right), \quad \mathbf{F}_4 = L\left(t + \Delta_t, \mathbf{F}^n + \Delta_t \cdot \mathbf{F}_3\right) \quad (2.9)$$

where $\mathbf{F} = (H_x, H_y, H_z, E_x, E_y, E_z)^T$.

The R-K method is high-order accurate and has a good stability in the time direction. However, it introduces amplitude error and consumes a large quantity of memory. To save the memory, E. Turkel improved the traditional R-K method [3] with a reduction of half memory. For nonlinear partial differential equations (PDEs), the improved R-K method is only second-order accurate. But it remains fourth-order accuracy for the linear Maxwell's equations.

2.1.1.2 Second-Order Leap-Frog (Staggered) Time-Stepping Approach [1]

The matrix L can be split into the summation of the matrices U and V , i.e.,

$$L = U + V \quad (2.10)$$

$$U = \begin{pmatrix} \{0\}_{3 \times 3} & -\frac{1}{\sqrt{\mu_0 \epsilon_0}} \mathfrak{R}_{3 \times 3} \\ \{0\}_{3 \times 3} & \{0\}_{3 \times 3} \end{pmatrix}, \quad V = \begin{pmatrix} \{0\}_{3 \times 3} & \{0\}_{3 \times 3} \\ \frac{1}{\sqrt{\mu_0 \epsilon_0}} \mathfrak{R}_{3 \times 3} & \{0\}_{3 \times 3} \end{pmatrix} \quad (2.11)$$

where U and V satisfy $U^\gamma = 0, \gamma \geq 2$, $V^\gamma = 0, \gamma \geq 2$, and $UV \neq VU$.

According to the matrix decomposition technique, we can rewrite the time evolution matrix $\exp(\Delta_t(U + V))$ as a product of matrices

$$\exp(\Delta_t(U + V)) \approx \exp\left(\frac{U\Delta_t}{2}\right) \cdot \exp(V\Delta_t) \cdot \exp\left(\frac{U\Delta_t}{2}\right) \quad (2.12)$$

We employ the Taylor series to expand each term of (2.12) and then arrive at

$$\exp\left(\frac{U\Delta_t}{2}\right) = I + \frac{U\Delta_t}{2}, \quad \exp(V\Delta_t) = I + V\Delta_t \quad (2.13)$$

where I is the unit matrix.

So (2.12) can be rewritten as

$$\exp(\Delta_t(U + V)) = \left(I + \frac{U\Delta_t}{2}\right) \cdot (I + V\Delta_t) \cdot \left(I + \frac{U\Delta_t}{2}\right) + O(\Delta t^2) \quad (2.14)$$

By recombining the first with the third terms of (2.14) and adopting the staggered time-stepping strategy, we obtain the well-known leap-frog time-stepping approach used in the traditional FDTD method. The approach is simple and requires only one iteration or stage in each time step. It has second-order accuracy, and thus the error will accumulate under a long-term simulation.

2.1.1.3 Unconditionally Stable Algorithms [7–11]

Similar to (2.12), we recast the time evolution matrix into

$$\exp(\Delta_t(U + V)) \approx \exp\left(\frac{V\Delta_t}{2}\right) \cdot \exp\left(\frac{U\Delta_t}{2}\right) \cdot \exp\left(\frac{U\Delta_t}{2}\right) \cdot \exp\left(\frac{V\Delta_t}{2}\right) \quad (2.15)$$

The Padé approximation is of form

$$\exp\left(\frac{V\Delta_t}{2}\right) = \frac{I}{I - (V\Delta_t)/2} \quad \exp\left(\frac{U\Delta_t}{2}\right) = \frac{I}{I - (U\Delta_t)/2} \quad (2.16)$$

Alternatively employing Taylor and Padé expansions, (2.15) can be changed to

$$\exp(\Delta_t(U + V)) = \left(\frac{I}{I - (V\Delta_t)/2}\right) \cdot \left(I + \frac{U\Delta_t}{2}\right) \cdot \left(\frac{I}{I - (U\Delta_t)/2}\right) \cdot \left(I + \frac{V\Delta_t}{2}\right) + O(\Delta t^2) \quad (2.17)$$

The alternating direction implicit (ADI) algorithm [7, 8] can efficiently simulate electrically small objects with a large time step and a small space step. Unfortunately, the computational complexity of the algorithm increases due to the implicit matrix inversion in each time step compared to other explicit methods. Furthermore, a larger time step will make the numerical dispersion of the ADI algorithm worse, which can be improved by the unconditionally stable Crank-Nicolson scheme [10] but with higher computational complexity. Recently, an unconditionally stable one-step algorithm [9] has been proposed based on the accurate solution of the time evolution matrix in the space or

spectral domain. Although it saves a lot of CPU time, the one-step algorithm is very difficult to handle inhomogeneous boundary conditions.

2.1.1.4 High-Order Symplectic Integration Scheme [12–15]

With the aid of the high-order decomposition technique of the exponential matrix, the time evolution matrix can be approximately reconstructed by the m -stage p th-order symplectic integrator. Here, the matrix corresponding to each stage is called the elementary symplectic mapping

$$\exp(\Delta_t(U + V)) = \prod_{l=1}^m \exp(d_l \Delta_t V) \exp(c_l \Delta_t U) + O(\Delta_t^{p+1}) \quad (2.18)$$

where c_l and d_l are the symplectic integrators or propagators.

The high-order symplectic integration scheme has desired numerical precision and high numerical stability but needs multiple stages in every time step. Compared with the R-K method, it has the energy-preserving property and saves memory.

2.1.2 Space Discretization Methods

Besides discretization strategies in the time domain, versatile space discretization methods are also proposed to approximate the spatial first-order derivatives.

2.1.2.1 Second-Order Leap-Frog (Staggered) Difference [1]

$$\left. \frac{\partial F}{\partial \delta} \right|_{\delta=h\Delta_\delta} = \frac{F(h+1/2) - F(h-1/2)}{\Delta_\delta} + O(\Delta_\delta^2) \quad \delta = x, y, z \quad h = i, j, k \quad (2.19)$$

where $F(h+1/2)$ denotes the value of F at $\delta = (h+1/2)\Delta_\delta$, and $\partial F / \partial \delta|_{\delta=h\Delta_\delta}$ denotes the first derivatives of F at $\delta = h\Delta_\delta$.

The second-order leap-frog (staggered) difference has advantages in terms of low complexity and natural parallelism. Meanwhile, it can model electromagnetic responses of inhomogeneous materials with curved boundaries by using local subgridding [16] and conformal techniques [17–21]. In view of a long-term or large-scale simulation, the method produces a significant numerical dispersion. Consequently, to accurately capture the wave physics of inhomogeneous scatterers, fine spatial grids should be adopted, which consumes a great number of computer resources.

2.1.2.2 Fourth-Order Staggered Difference [22–25]

$$\left. \frac{\partial F}{\partial \delta} \right|_{\delta=h\Delta_\delta} = \frac{9}{8} \times \frac{F(h+1/2) - F(h-1/2)}{\Delta_\delta} - \frac{1}{24} \times \frac{F(h+3/2) - F(h-3/2)}{\Delta_\delta} + O(\Delta_\delta^4) \quad (2.20)$$

The fourth-order staggered difference achieves much lower numerical dispersion compared to the second-order staggered difference and shows potential advantages in large-scale electromagnetic simulations. The main pitfalls of the method involve low stability and difficult treatments of inhomogeneous boundaries. The former can be improved by introducing the R-K method or the symplectic integration scheme. The latter can be improved by recently developed high-order conformal and subgridding techniques [14,26–29].

2.1.2.3 Fourth-Order Implicit Compact Difference Algorithm [5, 6]

$$\frac{\frac{\partial F}{\partial \delta} \Big|_{\delta=(h+1)\Delta\delta} + \frac{\partial F}{\partial \delta} \Big|_{\delta=(h-1)\Delta\delta}}{24} + \frac{11}{12} \frac{\partial F}{\partial \delta} \Big|_{\delta=h\Delta\delta} = \frac{F(h+1/2) - F(h-1/2)}{\Delta\delta} + (\Delta\delta^4) \quad (2.21)$$

The fourth-order implicit compact difference algorithm, which is more accurate than the fourth-order explicit staggered difference method, could employ the same conformal and subgridding techniques as the second-order explicit staggered difference. However, a tridiagonal matrix inversion is required for each time step, resulting in low computational efficiency.

2.1.2.4 Multiresolution Expansion Method [30]

$$\left(\frac{\partial F}{\partial \delta} \right)_h \approx \frac{1}{\Delta\delta} \int \psi_h(\delta) \frac{\partial \psi_{h+1/2}(\delta)}{\partial \delta} F_{h+1/2} d\delta \quad (2.22)$$

where $(\partial F/\partial \delta)_h$ denotes the derivatives of F along the δ direction, ψ is the scaling function in the wavelet theory, and $F_{h+1/2}$ denotes the sampling of F at the staggered grids.

The multiresolution expansion method saves a large quantity of memory and CPU time with drastically reduced sampling points per wavelength. Similar to the fourth-order staggered difference, it has low numerical stability and is not good at modeling inhomogeneous boundaries. The multiple image technique (MIT) [31] partially overcomes the difficulties in boundary treatments. However, the high-order precision of the multiresolution expansion method cannot be maintained.

2.1.2.5 Pseudo-Spectral Scheme [32]

$$\left(\frac{\partial F}{\partial \delta} \right)_h \approx \frac{2\pi}{N_\delta \Delta\delta} \xi_\delta^{-1} [j_0 h \cdot \xi_\delta (F_h)] \quad (2.23)$$

where ξ and ξ^{-1} respectively denote the forward and inverse operators of the centered discrete Fourier transform, F_h denotes the sampling of F at the

collocated grids, N_δ is the number of sampling points, and j_0 is the imaginary unit.

The pseudo-spectral scheme achieves the exponential convergence rate and remarkably lowers the complexity with coarse grids. The intrinsic weakness of the scheme lies at the Gibbs phenomena occurring at the inhomogeneous boundaries, which limits the application of the scheme.

From our personal views, a stable, accurate, fast, and efficient time-domain solver for Maxwell's equations can be proposed based on the following principles. First, one can design new methods to approximate the time evolution matrix or spatial first-order derivatives. Second, the proposed time-domain and space-domain algorithms can be recombined with each other. Third, these developed algorithms can be hybridized [33–35] with the finite-element time-domain [36], finite-volume time-domain [37] or discontinuous Galerkin time-domain methods [38].

2.2 Core Techniques

Nanoscience and technology become more and more important in cutting-edge industry. The advances in nanoscience and nanotechnology are attributed to newly acquired abilities to measure, fabricate, and manipulate individual structures on the nanometer scale. Controlling the light-matter interaction at the nanoscale is of paramount importance for emerging nanodevices and quantum devices. Photonics [39,40], plasmonics [41–47], and metamaterials [48–55] unprecedentedly change the traditional views and tools to control the propagation, radiation, and scattering of electromagnetic fields and to some extent break the diffraction limit in optics. Characterizing unique features, exploring new functionalities, and optimizing performances of nanostructures and nanodevices strongly depend on the rigorous solution of Maxwell's equations. As an accurate, fast, and efficient full-wave solver, the FDTD method can help to predict electromagnetic responses, understand working principles, reduce experimental costs, and shorten development periods of nano-optical designs. On one hand, the random, multilayered, and periodic nanostructures of interest have the inhomogeneous, dispersive, and anisotropic characteristics, presenting many challenges in developing the FDTD method. On the other hand, the large-scale simulation with broadband and wide-angle excitations requires huge computer resources and has to be tackled with the parallel FDTD technique. In this section, we will briefly describe core techniques of the FDTD method and particularly focus on those for nano-optics applications.

2.2.1 Basic Update Equations and Material Averaging Technique

Considering homogenous and isotropic media, the basic update equation of the FDTD method for the x component of the scaled electric field (E-field) is given by

$$\begin{aligned} \hat{E}_x^{n+1}\left(i+\frac{1}{2}, j, k\right) &= \hat{E}_x^n\left(i+\frac{1}{2}, j, k\right) + \frac{1}{\epsilon_r\left(i+\frac{1}{2}, j, k\right)} \\ &\times \left\{ \begin{aligned} &\alpha_y \times \left[H_z^{n+1/2}\left(i+\frac{1}{2}, j+\frac{1}{2}, k\right) - H_z^{n+1/2}\left(i+\frac{1}{2}, j-\frac{1}{2}, k\right) \right] \\ & - \alpha_z \times \left[H_y^{n+1/2}\left(i+\frac{1}{2}, j, k+\frac{1}{2}\right) - H_y^{n+1/2}\left(i+\frac{1}{2}, j, k-\frac{1}{2}\right) \right] \end{aligned} \right\} \end{aligned} \quad (2.24)$$

$$\alpha_y = \frac{1}{\sqrt{\mu_0 \epsilon_0}} \frac{\Delta_t}{\Delta_y}, \quad \alpha_z = \frac{1}{\sqrt{\mu_0 \epsilon_0}} \frac{\Delta_t}{\Delta_z} \quad (2.25)$$

where ϵ_r is the relative permittivity. Similarly, the update equation for the y component of the magnetic field (H-field) is of form

$$\begin{aligned} H_y^{n+1/2}\left(i+\frac{1}{2}, j, k+\frac{1}{2}\right) &= H_y^{n-1/2}\left(i+\frac{1}{2}, j, k+\frac{1}{2}\right) + \frac{1}{\mu_r\left(i+\frac{1}{2}, j, k+\frac{1}{2}\right)} \\ &\times \left\{ \begin{aligned} &\alpha_x \times \left[\hat{E}_z^n\left(i+1, j, k+\frac{1}{2}\right) - \hat{E}_z^n\left(i, j, k+\frac{1}{2}\right) \right] \\ & - \alpha_z \times \left[\hat{E}_x^n\left(i+\frac{1}{2}, j, k+1\right) - \hat{E}_x^n\left(i+\frac{1}{2}, j, k\right) \right] \end{aligned} \right\} \end{aligned} \quad (2.26)$$

$$\alpha_x = \frac{1}{\sqrt{\mu_0 \epsilon_0}} \frac{\Delta_t}{\Delta_x} \quad (2.27)$$

where μ_r is the relative permeability. For the lossy media (take \hat{E}_x component as an example), the iteration equation can be rewritten as

$$\begin{aligned} \hat{E}_x^{n+1}\left(i+\frac{1}{2}, j, k\right) &= \exp(-\xi) \times \hat{E}_x^n\left(i+\frac{1}{2}, j, k\right) \\ &+ \frac{1-\exp(-\xi)}{\xi} \times \frac{1}{\varepsilon_r\left(i+\frac{1}{2}, j, k\right)} \\ &\times \left\{ \begin{aligned} &\alpha_y \times \left[H_z^{n+1/2}\left(i+\frac{1}{2}, j+\frac{1}{2}, k\right) - H_z^{n+1/2}\left(i+\frac{1}{2}, j-\frac{1}{2}, k\right) \right] \\ &-\alpha_z \times \left[H_y^{n+1/2}\left(i+\frac{1}{2}, j, k+\frac{1}{2}\right) - H_y^{n+1/2}\left(i+\frac{1}{2}, j, k-\frac{1}{2}\right) \right] \end{aligned} \right\} \end{aligned} \quad (2.28)$$

where

$$\xi = \frac{\Delta_t \sigma\left(i+\frac{1}{2}, j, k\right)}{\varepsilon\left(i+\frac{1}{2}, j, k\right)},$$

and σ is the electric conductivity. For the exponential functions, we can employ the Padé expansion to access their values, i.e.,

$$\exp(-\xi) = \frac{1 - \frac{\xi}{2} + \frac{\xi^2}{12}}{1 + \frac{\xi}{2} + \frac{\xi^2}{12}} + O(\xi^5), \quad \frac{1 - \exp(-\xi)}{\xi} = \frac{1 - \frac{\xi}{10} + \frac{\xi^2}{60}}{1 + \frac{2\xi}{5} + \frac{\xi^2}{20}} + O(\xi^5) \quad (2.29)$$

For inhomogeneous nonmagnetic media, which are always modeled in nano-optics problems, the above constitutive parameters can be averaged as

$$\bar{\varepsilon}_r = \frac{1}{A_S} \iint_S \varepsilon_r dS, \quad \bar{\sigma} = \frac{1}{A_S} \iint_S \sigma dS \quad (2.30)$$

where S is the surface corresponding to the E-field component enclosed by the four H-field components, A_S is the area of S , and $\bar{\varepsilon}_r$ and $\bar{\sigma}$ are the averaged relative permittivity and electric conductivity, respectively. The integrals (2.30) can be converted into the summation forms according to the subgridding techniques [4,14].

2.2.2 Absorbing Boundary Condition

Because of limited computer resources, an absorbing boundary condition is compulsory to truncate the infinite free space (or air region) for simulating the optical radiation and scattering from nanoscatterers. The perfectly matched layer (PML) [56,57] is able to absorb the outgoing waves without spurious reflections and to perfectly simulate unbounded wave propagations.

Using the split-field technique, we decompose the x polarized E-field into two subcomponents propagating along the y - and z -directions, respectively.

$$\hat{E}_x = \hat{E}_{xy} + \hat{E}_{xz} \quad (2.31)$$

The update equation of the subcomponent propagating along the y -direction is written as

$$\begin{aligned} \hat{E}_{xy}^{n+1}\left(i + \frac{1}{2}, j, k\right) &= \exp(-\xi) \times \hat{E}_{xy}^n\left(i + \frac{1}{2}, j, k\right) + \frac{1 - \exp(-\xi)}{\xi} \\ &\times \alpha_y \times \left[H_z^{n+1/2}\left(i + \frac{1}{2}, j + \frac{1}{2}, k\right) - H_z^{n+1/2}\left(i + \frac{1}{2}, j - \frac{1}{2}, k\right) \right] \end{aligned} \quad (2.32)$$

where

$$\xi = \frac{\Delta_t \sigma_y\left(i + \frac{1}{2}, j, k\right)}{\epsilon_0}$$

Likewise, the update equation of the subcomponent propagating along the z -direction is given by

$$\begin{aligned} \hat{E}_{xz}^{n+1}\left(i + \frac{1}{2}, j, k\right) &= \exp(-\xi) \times \hat{E}_{xz}^n\left(i + \frac{1}{2}, j, k\right) - \frac{1 - \exp(-\xi)}{\xi} \\ &\times \alpha_z \times \left[H_y^{n+1/2}\left(i + \frac{1}{2}, j, k + \frac{1}{2}\right) - H_y^{n+1/2}\left(i + \frac{1}{2}, j, k - \frac{1}{2}\right) \right] \end{aligned} \quad (2.33)$$

where

$$\xi = \frac{\Delta_t \sigma_z\left(i + \frac{1}{2}, j, k\right)}{\epsilon_0}$$

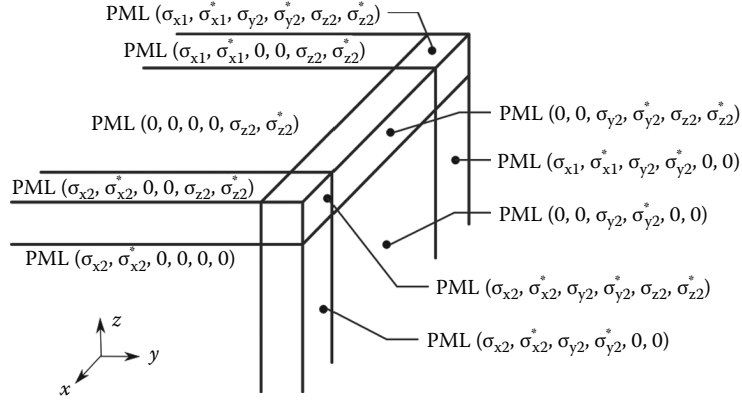


FIGURE 2.1

The settings of electric and magnetic conductivities in the PMLs.

To reduce the spurious numerical reflection, the electric conductivity can be set as the following polynomial form, i.e.,

$$\sigma(\Lambda) = \sigma_{\max} \left(\frac{\Lambda}{\Gamma} \right)^\kappa \quad (2.34)$$

where Λ is the distance from the PML-air interface, Γ is the thickness of the PMLs, σ_{\max} is the maximum electric conductivity, and κ is the order of the polynomial. Besides the \hat{E}_x component, all the other components should use the split-field technique also. To absorb the outgoing waves from different directions, the settings of the electric and magnetic conductivities in the PMLs are shown in Figure 2.1. Additionally, an easier and more elegant technique to implement the PML, called convolution PML (CPML), can be found in [58].

2.2.3 Source Excitations

The typical source excitations in the FDTD solution include the plane wave and point (dipole) sources.

A rigorous way of introducing the plane wave excitation is to use the total-field and scattered-field (TF-SF) technique [2]. We assume that the E-field is x-polarized and propagates along the z-direction. The total-field region occupies $[i_1, i_2] \times [j_1, j_2] \times [k_1, k_2]$. The additional update equation of \hat{E}_x field at the $k = k_1$ plane is of form

$$\hat{E}_x^{n+1} \left(i + \frac{1}{2}, j, k_1 \right) = \hat{E}_x^n \left(i + \frac{1}{2}, j, k_1 \right) + \alpha_z \times H_{y,inc}^{n+1/2} \left(k_1 - \frac{1}{2} \right) \quad (2.35)$$

At the $k = k_2$ plane, the additional update equation of \hat{E}_x field is given by

$$\hat{E}_x^{n+1}\left(i + \frac{1}{2}, j, k_2\right) = \hat{E}_x^n\left(i + \frac{1}{2}, j, k_2\right) - \alpha_z \times H_{y,inc}^{n+1/2}\left(k_2 + \frac{1}{2}\right) \quad (2.36)$$

where $i_1 \leq i \leq i_2 - 1$, $j_1 \leq j \leq j_2$, and $H_{y,inc}$ is the incident H-field. We can modify the iterations of \hat{E}_z , H_y , and H_z components at the TF-SF interfaces accordingly through introducing the equivalent incident sources. In view of the incident source, the one-dimensional (1D) FDTD method can be employed. For example, $\hat{E}_{x,inc}$ can be updated by

$$\hat{E}_{x,inc}^{n+1}(k) = \hat{E}_{x,inc}^n(k) - \alpha_z \times \left[H_{y,inc}^{n+1/2}\left(k + \frac{1}{2}\right) - H_{y,inc}^{n+1/2}\left(k - \frac{1}{2}\right) \right] \quad (2.37)$$

At the $k = k_s$ point, the source $\zeta(t)$ is added as

$$\hat{E}_{x,inc}^{n+1}(k_s) = \zeta^{n+1}((n+1)\Delta_t) \quad (2.38)$$

where

$$\zeta(t) = -\cos(\omega t) \exp\left(-\frac{4\pi(t - T_0)^2}{W^2}\right) \quad (2.39)$$

with an effective frequency range $f \in [\omega / 2\pi - 2/W, \omega / 2\pi + 2/W]$ and $T_0 = 9\pi/2\omega$. Alternatively, the plane wave incidence can be approximately realized by exciting a transparent or soft source at a planar surface. One can place the planar source along one of the inner PML boundaries (see Figure 2.2). Make sure that the size of the source is the same as that of the entire simulation cell (including the PML thickness) along its planar dimension. Under this situation,

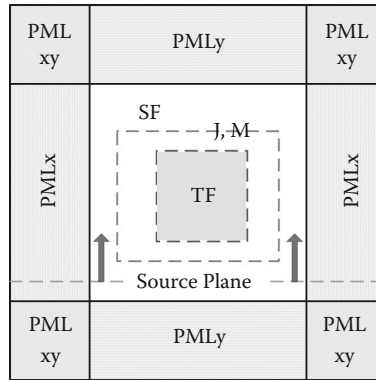


FIGURE 2.2

The 2D FDTD configurations involving the perfectly matched layers (PMLs), total-field (TF) region, scattered-field (SF) region, planar source plane, and equivalent currents J and M for the near-to-far-field (NFF) transformation.

the entire computational domain becomes the total-field region, and thus there is no scattered-field region. The scattered fields can be obtained by extracting the incident fields from the total fields by running the FDTD program twice.

The dipole source is essential to predict the emission of atoms, molecules, and quantum dots in inhomogeneous environments. It can be used for analyzing the spontaneous emission [59–62], near-field heat transfer [63–65], Casimir force [66–68], solar cells [69], and so on. The electromagnetic radiation of a point source relates to the local density of states (LDOS) concept [42], which plays a fundamental role in modern physics. The dipole source is implemented as follows:

$$\hat{E}_x^{n+1}(k_s) = \hat{E}_x^n(k_s) - \frac{\Delta_t}{\epsilon_0 \delta^3} \left[\frac{dp}{dt} \right]^{n+1/2} \quad (2.40)$$

where $p = A \exp[-4\pi((t - T_0)/W)^2]$ corresponds to the dipole momentum and $\delta^3 = \Delta_x \Delta_y \Delta_z$ is the volume of a Yee cell. In fact, the transparent source adopted is the differential Gaussian pulse without the direct current (DC) component. The LDOS, which counts the number of electromagnetic modes where photons can be emitted at the specific location of the emitter, can be calculated by the superposition of the projected LDOS. The projected (per-polarization) LDOS is exactly proportional to the power radiated by an l -oriented point-dipole current $J(\omega)$ at the given position in space [70]:

$$\text{LDOS}(\mathbf{r}, \omega) = \frac{-2}{\pi} \epsilon(\mathbf{r}) \frac{\text{Re} \left[\tilde{E}_l(\mathbf{r}, \omega) \tilde{J}(\omega) \right]}{|\tilde{J}(\omega)|^2} \quad (2.41)$$

where the normalization of $|\tilde{J}(\omega)|^2$ is necessary for obtaining the power exerted by a unit-amplitude Hertzian dipole.

The eigenvalue problem is fundamentally important in the nano-optics field. On one hand, the excitation solution by the plane wave or dipole sources can be expanded in terms of dominant eigenmodes. On the other hand, the dispersion diagram or relation generated provides key characteristics of an electromagnetic system involving the group velocity, quality factor, and density of states (DOS). To excite all possible resonant modes in the electromagnetic system, we set the initial condition for all the E-field components, taking the z component as an example [71]:

$$\hat{E}_z^0 \left(i, j, k + \frac{1}{2} \right) = \exp \left[-\frac{(i - i_c)^2 + (j - j_c)^2}{2\tau_g^2} \right] \quad (2.42)$$

where i_c, j_c, k_c are the center points of the system, τ_g is the width of the spatial pulse, and i, j, k can be set as $i > i_c, j > j_c,$ and $k > k_c$. The asymmetric setup enables all the eigenmodes to be excited.

2.2.4 Near-to-Far-Field Transformation

To obtain far-field scattering or radiation information, the near-to-far-field (NFF) transformation [2] should be implemented at a closed surface enclosing the scatterers. The E-field and H-field values at the closed surface in the frequency domain should be evaluated via the discrete Fourier transform or fast Fourier transform before the NFF transformation.

The discrete Fourier transform for the scaled \tilde{E}_x field is described as

$$\tilde{E}_x(f) = \sum_{n=0}^{n_{\max}} \hat{E}_x^n(n\Delta_t) \exp(-j_0 2\pi f n\Delta_t) \quad (2.43)$$

where \tilde{E} is the scaled E-field in the frequency domain, and n_{\max} is the required time steps before the steady state is reached. The equivalent electric current $\tilde{\mathbf{J}}$ and magnetic current $\tilde{\mathbf{J}}_m$ are respectively defined by

$$\tilde{\mathbf{J}} = \mathbf{n} \times \tilde{\mathbf{H}}, \quad \tilde{\mathbf{J}}_m = -\mathbf{n} \times \tilde{\mathbf{E}} \quad (2.44)$$

where \mathbf{n} is the outer normal vector of the closed surface. With the help of the equivalent principle, the E-field in the far-field zone can be calculated by

$$\begin{aligned} \tilde{E}_\theta = -j_0 k_0 \frac{\exp(-j_0 k_0 r)}{4\pi r} & \left[(\tilde{f}_x \cos \theta \cos \varphi + \tilde{f}_y \cos \theta \sin \varphi - \tilde{f}_z \sin \theta) \right. \\ & \left. + (-\tilde{f}_{mx} \sin \varphi + \tilde{f}_{my} \cos \varphi) \right] \end{aligned} \quad (2.45)$$

$$\begin{aligned} \tilde{E}_\varphi = j_0 k_0 \frac{\exp(-j_0 k_0 r)}{4\pi r} & \left[(\tilde{f}_{mx} \cos \theta \cos \varphi + \tilde{f}_{my} \cos \theta \sin \varphi - \tilde{f}_{mz} \sin \theta) \right. \\ & \left. + (\tilde{f}_x \sin \varphi - \tilde{f}_y \cos \varphi) \right] \end{aligned} \quad (2.46)$$

$$\tilde{f}_\delta = \iint_A \tilde{J}_\delta(r') \exp[j_0 k_0 (x' \sin \theta \cos \varphi + y' \sin \theta \sin \varphi + z' \cos \theta)] ds' \quad (2.47)$$

$$\tilde{f}_{m\delta} = \iint_A \tilde{J}_{m\delta}(r') \exp[j_0 k_0 (x' \sin \theta \cos \varphi + y' \sin \theta \sin \varphi + z' \cos \theta)] ds' \quad (2.48)$$

where k_0 is the wave number of free space, r is the distance from the source to the field points, $\iint_A ds'$ denotes the area integral in the whole closed surface, and θ and φ are the spherical angles.

2.2.5 Periodic Structures

A periodic structure has profound theoretical meanings and practical uses in nanoscience and technology. It can be made from dielectrics, metals, and

their hybrids with structured lattices. The periodic structure is crucial for optical components and devices, such as nanoantennas [72], nanocircuits (waveguides, polarizers, filters) [40, 73–75], and optoelectronics (solar cells, light-emitting diodes, and lasers) [45, 76–79]. First, due to the constructive and destructive interferences, the period structures could open up a band gap where the photon emission is forbidden or inhibited and form a band edge where the light intensity is extremely enhanced [39, 40]. Second, the group delay of modulated optical signals is also highly tunable in the slow-wave structure [80,81]. Third, periodic structures could control the emission direction of atoms, molecules, and quantum dots by the diffraction effect of Floquet modes [82,83]. Finally, the interferences between the quasi-guided mode of periodic structures and incident light induce many interesting physical phenomena involving the Fano-resonance or Wood's anomaly [84–86], electromagnetically induced transparency [87], and so on. In sum, modeling periodic structures and unveiling relevant physical mechanisms have a high impact in the nano-optics field. The challenges in the FDTD method to model periodic structures can be understood from the Bloch theorem:

$$\tilde{\mathbf{E}}(\mathbf{r} + \mathbf{R}) = \tilde{\mathbf{E}}(\mathbf{r}) \exp(-j_0 \mathbf{k}_B \cdot \mathbf{R}) \quad (2.49)$$

$$\tilde{\mathbf{E}}(\mathbf{r}) = \tilde{\mathbf{E}}(\mathbf{r} + \mathbf{R}) \exp(j_0 \mathbf{k}_B \cdot \mathbf{R}) \quad (2.50)$$

where \mathbf{k}_B is the Bloch wave vector.

In the time domain, (2.49) can be numerically implemented because $\tilde{\mathbf{E}}(\mathbf{r} + \mathbf{R})$ has a time delay (or retardation) with respect to $\tilde{\mathbf{E}}(\mathbf{r})$. However, the anti-causal property can be found in (2.50). The value of $\tilde{\mathbf{E}}(\mathbf{r})$ at the current time step depends on that of $\tilde{\mathbf{E}}(\mathbf{r} + \mathbf{R})$ at the following time step, which is unknown physically. Here we implement periodic boundary conditions in the time domain by the constant horizontal wave number approach [88] with complex field values. Although the memory cost of the FDTD method will double, the phase delay in periodic boundary conditions (PBCs) can be incorporated conveniently.

For example, to update \hat{E}_x field on the periodic boundary, the value of H_z component outside the unit cell is needed. Fortunately, assuming the periodicity in the y -direction, one can use the H_z component of interest inside the unit cell to update the E-field, such that

$$\begin{aligned} \hat{E}_x^{n+1} \left(i + \frac{1}{2}, 0, k \right) &= \hat{E}_x^n \left(i + \frac{1}{2}, 0, k \right) + \frac{1}{\epsilon_r \left(i + \frac{1}{2}, 0, k \right)} \\ &\times \left\{ \begin{aligned} &\alpha_y \times \left[H_z^{n+1/2} \left(i + \frac{1}{2}, \frac{1}{2}, k \right) - H_z^{n+1/2} \left(i + \frac{1}{2}, n_y - \frac{1}{2}, k \right) \times \exp(jk_y P_y) \right] \\ &- \alpha_z \times \left[H_y^{n+1/2} \left(i + \frac{1}{2}, 0, k + \frac{1}{2} \right) - H_y^{n+1/2} \left(i + \frac{1}{2}, 0, k - \frac{1}{2} \right) \right] \end{aligned} \right\} \quad (2.51) \end{aligned}$$

where P_y and k_y are, respectively, the periodicity and Bloch wave number along the y -direction. The TF-SF technique is not applicable to implement the plane wave source for periodic structures, and the pure total-field technique should be employed with a transparent source at the excitation plane, which has been described in the “source excitations” subsection. The incident angle of the plane wave can be controlled by changing the value of k_y . There exists a problem of horizontal resonance [88], where fields do not decay to zero over time. To avoid this problem, the proper frequency range for the excitation waveform must be chosen as follows:

$$f_c = \frac{k_y c}{2\pi} + \frac{BW}{2} \quad (2.52)$$

where f_c is the center frequency of the Gaussian pulse and BW is the corresponding bandwidth. The constant horizontal wave number approach can be naturally extended to the skewed grid periodic structures with a simple linear interpolation [88].

2.2.6 Dispersive Media

In the nano-optics field, most materials are dispersive with a frequency-dependent complex permittivity. Debye, Lorentz, and Drude media are three main classes of dispersive materials and have different frequency-dependent behaviors. Various techniques have been developed to model these dispersive materials, such as the recursive convolution (RC) [89], the auxiliary differential equation (ADE) [90], piecewise linear recursive convolution [91], and the Z-transform methods [92]. Mathematically, we can use several Lorentz terms with different harmonic resonances to represent the permittivity of an arbitrary dispersive material, i.e.,

$$\epsilon(\omega) = \epsilon_\infty + \sum_n \frac{\beta_n \omega_n^2}{\omega_n^2 - \omega^2 + j\omega\gamma_n} \quad (2.53)$$

where the first term is the instantaneous dielectric function corresponding to the infinite-frequency response and the Lorentz terms are related to the frequency-dependent polarization density in the material

$$\mathbf{D} = \epsilon \mathbf{E} = \epsilon_\infty \mathbf{E} + \mathbf{P} \quad (2.54)$$

$$\mathbf{P} = \sum_n \mathbf{P}_n \quad (2.55)$$

$$\frac{d^2 \mathbf{P}_n}{dt^2} + \gamma_n \frac{d\mathbf{P}_n}{dt} + \omega_n^2 \mathbf{P}_n = \beta_n \omega_n^2 \mathbf{E} \quad (2.56)$$

For a practical curve fitting process, we must force $\omega_n \Delta t / 2 \leq 1$ to ensure the stability of the algorithm and β_n also cannot be too large.

The Ampere's law in the time domain can be expressed as

$$\nabla \times H = \epsilon_\infty \frac{d}{dt} \mathbf{E}(t) + \sigma \mathbf{E}(t) + \sum_p \mathbf{J}_p(t) \quad (2.57)$$

where \mathbf{J}_p are the polarization currents satisfying

$$\frac{d^2 \mathbf{J}_p}{dt^2} + \gamma_n \frac{d \mathbf{J}_p}{dt} + \omega_n^2 \mathbf{J}_p = \beta_n \omega_n^2 \frac{d \mathbf{E}}{dt} \quad (2.58)$$

Using the ADE technique, we discretize the differential equation (2.58) with centered differences

$$\frac{\mathbf{J}_p^{n+1} - 2\mathbf{J}_p^n + \mathbf{J}_p^{n-1}}{\Delta t^2} + \gamma_n \frac{\mathbf{J}_p^{n+1} - \mathbf{J}_p^{n-1}}{2\Delta t} + \omega_n^2 \mathbf{J}_p^n = \beta_n \omega_n^2 \frac{\mathbf{E}^{n+1} - \mathbf{E}^{n-1}}{2\Delta t} \quad (2.59)$$

From the ADE, we can obtain the polarization current \mathbf{J}_p at the $(n+1)$ th time step by those at the n th and $(n-1)$ th. Considering that we require the polarization current at the $(n+1/2)$ th time step from (2.57), a simple linear interpolation can be adopted:

$$\mathbf{J}_p^{n+1/2} = \frac{1}{2} [\mathbf{J}_p^n + \mathbf{J}_p^{n+1}] \quad (2.60)$$

Substituting (2.59) and (2.60) into (2.57), we can get the update equation of E-field components. Starting with the known (stored) component values of \mathbf{E}^{n-1} , \mathbf{E}^n , \mathbf{J}_p^{n-1} , \mathbf{J}_p^n and $\mathbf{H}^{n+1/2}$, we calculate the new \mathbf{E}^{n+1} components. Then, we get the new \mathbf{J}_p^{n+1} components by using the just-computed \mathbf{E}^{n+1} components.

2.3 Numerical Examples for Nano-Optics Applications

Having unique features of tunable resonance and unprecedented near-field concentration, plasmon is an enabling technique for light manipulation and management [41–47]. By altering the metallic nanostructure, the properties of plasmons, in particular their interactions with light, can be tailored, which offers the potential for developing emerging optical components and devices. Meanwhile, the use of metallic materials with a negative permittivity is one of the most feasible ways of circumventing the fundamental (half-wavelength) limit and achieving localization of electromagnetic energy (at

optical frequencies) into nanoscale. In this section, we will investigate and explore plasmonic effects in various nano-optics applications.

2.3.1 Thin-Film Solar Cells

Solar cells [93,94], which can provide renewable and clean energy by converting the sunlight to electrical power, have attracted much attention in the past few years. Despite the growing importance, we need to reduce the cost of solar cells and increase the power conversion efficiency (PCE) before they can successfully replace fossil fuels for electrical power generation. A light-trapping scheme can realize the above two goals simultaneously and thus is useful for emerging solar cell technology meeting clean energy demands. As an efficient light-trapping technique [45], surface plasmons are collective oscillations of free electrons in metals that are confined to the surface between the metal and dielectric and interact strongly with light. The extremely near-field enhancement inherent from surface plasmons allows us to significantly improve the optical absorption of thin-film solar cells.

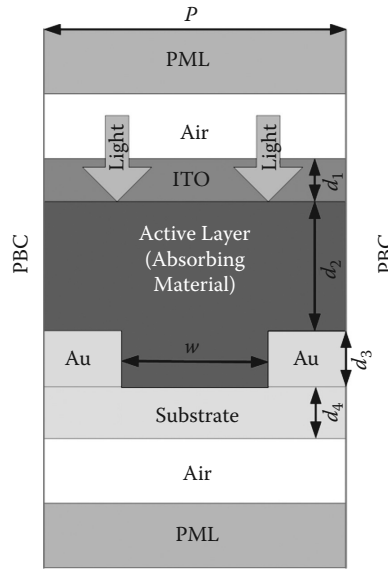
Here, we use the FDTD method to simulate a typical thin-film solar cell nanostructure in the literature [78]. Figure 2.3 shows the unit cell of the plasmonic thin-film solar cell. The incident wave is a p -polarized plane wave propagating vertically into the plasmonic solar cell. The ADE technique and Lorenz models are adopted for simulating the dispersive materials involving the absorbing material (amorphous silicon, A-Si) and metal (Au). The frequency-domain values of E-fields are obtained by the discrete (fast) Fourier transform. The real and imaginary parts of permittivities for the A-Si and Au are depicted in Figure 2.4. The complex permittivity of Au can be expressed by the Brendel-Bormann model [95] and that of A-Si is taken from [96]. The relative permittivities of ITO and SiO₂ are 4.0 and 2.1, respectively.

The electron-hole pair generation of solar cells depends on the photon energy absorbed by the absorbing material per unit time per unit area, i.e.,

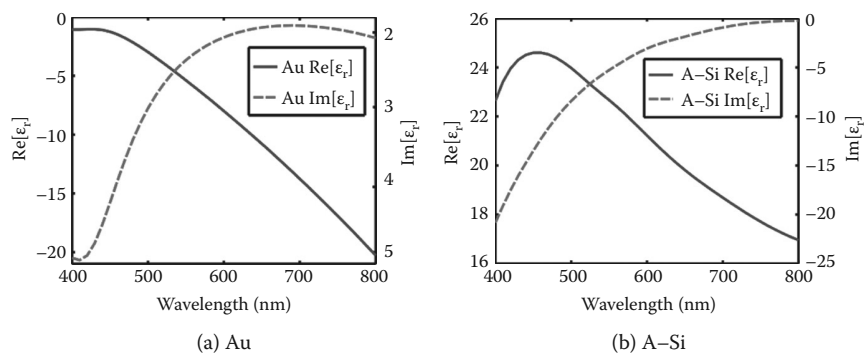
$$\eta = \frac{\int_S \sigma(\omega) |\tilde{\mathbf{E}}(\omega, \mathbf{r})|^2 dS}{\Delta_S} = \frac{-\omega \epsilon_0 \int_S \text{Im}[\epsilon_r(\omega)] |\tilde{\mathbf{E}}(\omega, \mathbf{r})|^2 dS}{\Delta_S} \quad (2.61)$$

where η is the power density, S denotes the region of the absorbing material, Δ_S is the area of S , and $\sigma(\omega) = -\omega \epsilon_0 \text{Im}[\epsilon_r(\omega)]$ is the conductivity of the absorbing material. Figure 2.6 shows the absorbed power density of the A-Si layer. Using the planar Au layer, the non-strip (planar) structure is also modeled. For the non-strip structure, $d_2 = 140$ nm is adopted for achieving the same A-Si area while other parameters are unchanged. The momentum of surface plasmons [41] is given by

$$k_{sp} = k_0 \sqrt{\frac{\epsilon_m \epsilon_a}{\epsilon_m + \epsilon_a}} \quad (2.62)$$

**FIGURE 2.3**

The unit cell of the plasmonic thin-film solar cell. The four-layered structure includes the indium tin oxide (ITO), active layer (absorbing material of amorphous silicon), metal (Au) electrodes, and substrate (SiO_2) with thicknesses of d_1 , d_2 , d_3 , and d_4 , respectively. The distance between two adjacent strips is w and the periodicity is P . The incident light propagates into the structure through the ITO. The PMLs are employed at the top and the bottom of the solar cell structure. The PBCs at the left and right sides of the unit cell are imposed. The geometric parameters of the device are set as $d_1 = 25$ nm, $d_2 = 120$ nm, $d_3 = 40$ nm, $d_4 = 30$ nm, $w = 100$ nm, and $P = 200$ nm.

**FIGURE 2.4**

The real and imaginary parts of relative permittivities for (a) Au and (b) A-Si.

where ϵ_m and ϵ_a are the permittivities of metal and absorbing material, respectively. It is well known that surface plasmons will exist if the condition $\text{Re}(-\epsilon_m) > \text{Re}(\epsilon_a)$ is satisfied. Thus the momentum of surface plasmons k_{sp} is larger than free space momentum k_0 of the plane wave (sunlight). Hence, additional momentum should be provided for exciting the surface plasmon. From Figure 2.6, the periodic strip incorporated solar cell shows much stronger absorption due to the excited surface plasmons. However, for the non-strip structure, the surface plasmons cannot be excited due to the momentum mismatch. The reflection coefficient results as presented in Figure 2.5 not only validate the FDTD results but also confirm the strong optical absorption of A-Si from 660 to 800 nm. The surface plasmon is successfully excited by the nanostrip as shown in Figure 2.7(b) in comparison with Figure 2.7(d). According to the mode conversion theory, the subwavelength strip can excite evanescent wave components, which may provide additional momentum. Furthermore, the Floquet modes supported by the periodic strip structure can also overcome the momentum mismatch problem. The waveguide mode also enhances the optical absorption of solar cells as illustrated in Figures 2.7(a) and (c). Particularly, the surface plasmon mode can be coupled to the waveguide mode or Floquet mode, which has a great help for boosting the absorption (Figure 2.7[b]).

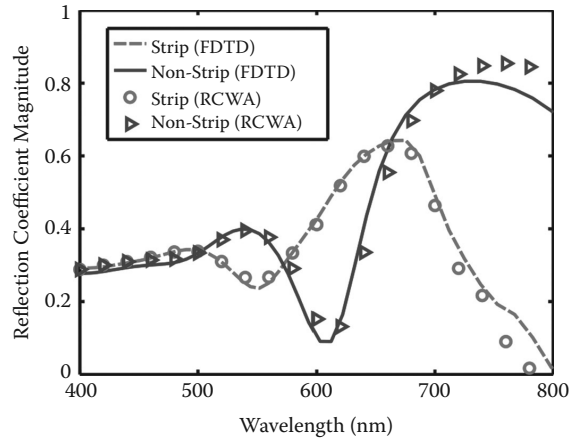


FIGURE 2.5

The reflection coefficients of the strip and non-strip solar cell architectures calculated by the FDTD method and rigorous coupled-wave analysis (RCWA) [97]. The pattern of the strip structure is shown in Figure 2.3. By using the planar Au layer, the non-strip structure has the same geometric size as the strip one except that $d_2 = 140$ nm is adopted for achieving the same A-Si area.

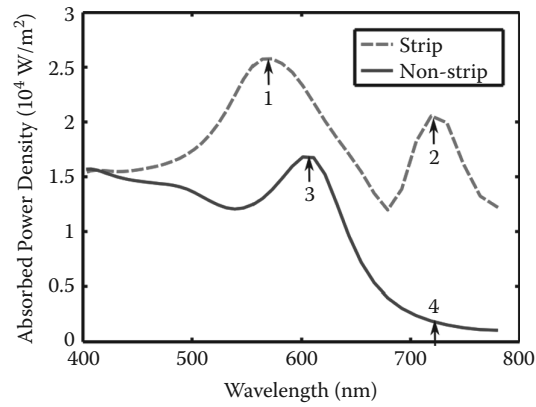


FIGURE 2.6
The absorbed power density of the active (A-Si) layer.

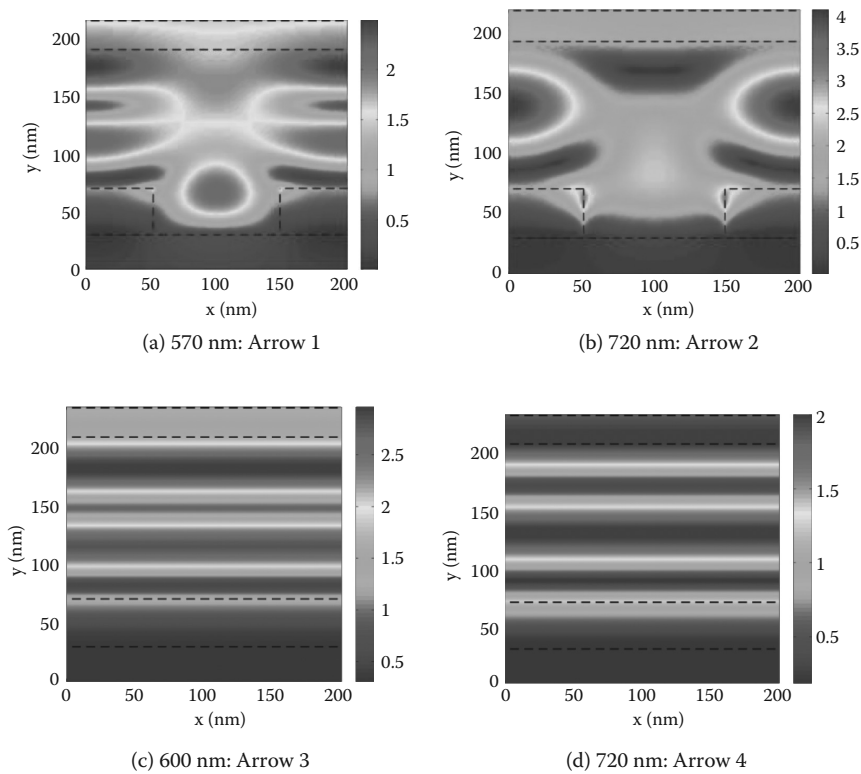


FIGURE 2.7
The near-field distributions for the absorption peaks of A-Si material denoted in Figure 2.6. (See color figure.)

2.3.2 Nanoantennas

Nanoantennas [72, 75, 98–103] play a fundamental role in nanotechnology due to their capabilities to confine and enhance the light through converting the localized to propagating electromagnetic fields, and vice versa. The nanoantenna is a direct analogue and extended technology of the radio wave and microwave antenna. But the nanoantenna possesses lots of individual and novel features mainly owing to the existence of the electron gas oscillations in metals. The behavior of strongly coupled plasmas and the capability of manipulating light on the nanometer scale make nanoantenna particularly useful in microscopy and spectroscopy [104], fluorescence enhancement [101], surface-enhanced Raman spectroscopy [105], and photovoltaics [106,107]. The above applications mainly rely on the characteristics of nanoantennas, such as the resonance frequency, bandwidth, directivity, far-field radiation pattern, near-field distribution, and local density of states. Here, we use the FDTD method to simulate a typical dipole nanoantenna with the schematic pattern shown in Figure 2.8. The relative permittivity of Al_2O_3 is 3.065 and the excitation source is a plane wave polarized along the arm direction of the antenna. Figure 2.9 demonstrates that the resonance frequency of the antenna can be tunable in a wide range by changing the arm length of the antenna. The absorption cross section can be defined by

$$\sigma_a = \frac{-\int_S \frac{1}{2} \text{Re} \left\{ \tilde{\mathbf{E}}(\omega, \mathbf{r}) \times \text{conj}[\tilde{\mathbf{H}}(\omega, \mathbf{r})] \right\} \cdot d\mathbf{S}}{|\tilde{\mathbf{S}}_i|} = \frac{-\int_S k_0 \text{Im}[\epsilon_r(\omega)] |\tilde{\mathbf{E}}(\omega, \mathbf{r})|^2 dS}{|\tilde{\mathbf{E}}_i|^2} \quad (2.63)$$

where *conj* denotes the complex conjugation, S is an arbitrary surface enclosing the nanoantenna, and $\mathbf{S}_i = \frac{1}{2} \text{Re}[\tilde{\mathbf{E}}_i \times \text{conj}(\tilde{\mathbf{H}}_i)]$ is the incident energy flux. The radar cross sections—i.e., radiation patterns from the reciprocal theorem—at the resonance and off the resonance of the antenna are shown in Figure 2.10. Both the absorption cross section and radar cross section are

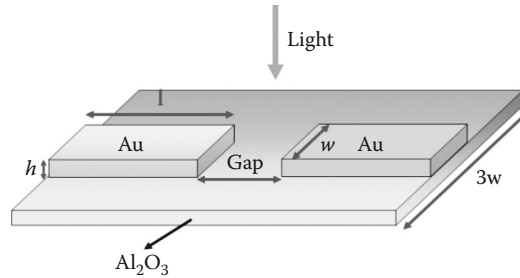


FIGURE 2.8

The schematic pattern of the metallic (Au) dipole nanoantenna with the Al_2O_3 as a substrate. The geometric size of the antenna is $l = 60$ nm, $w = 40$ nm, $h = 40$ nm, and $\text{Gap} = 20$ nm.

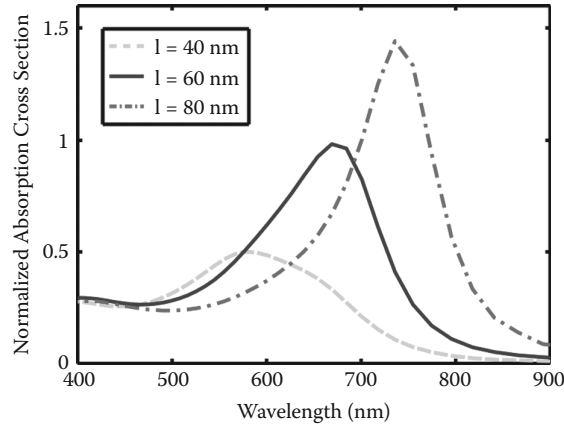


FIGURE 2.9 The normalized absorption cross sections of the dipole nanoantenna with varying arm lengths. The plasmonic resonance will be red-shifted and becomes stronger with the increasing arm length.

normalized with the geometric cross section area of the metallic dipole antenna ($2 \times l \times w$). At the resonance frequency, the radiation pattern of the dipole antenna is shaped like the well-known cosine square law, which is different from an asymmetric radiation pattern off the resonance. Moreover, the concentrated E-fields at the gap of the nanoantenna can be clearly observed

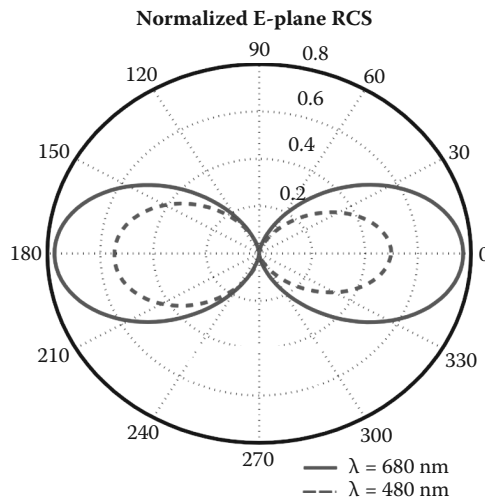
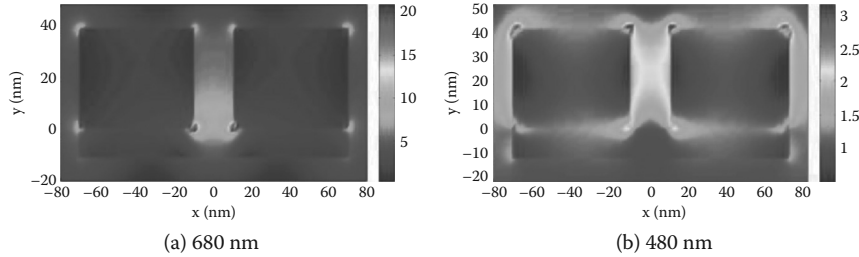


FIGURE 2.10 The normalized E-plane radar cross sections (RCSs) of the antenna respectively at the resonance (680 nm) and off the resonance (480 nm).

**FIGURE 2.11**

The near-field distributions of the antenna respectively at the resonance (680 nm) and off the resonance (480 nm). (See color figure.)

in Figure 2.11. The amplitude of the E-field at the resonance is significantly larger than that off the resonance (see colorbar).

2.3.3 Spontaneous Emissions

Control of spontaneously emitted light lies at the heart of quantum optics. It is also essential for diverse applications ranging from lasers, light-emitting diodes, and quantum information [59–62, 108]. It is well known that the radiation dynamics of an atom strongly depends on its environment, which was first discovered by Purcell [109], and the spontaneous emission (SE) can be enhanced if the emitting atom is coupled to a cavity resonator. According to the quantum electrodynamics theory, the SE of an atom can be a weak-coupling radiation process due to the vacuum fluctuations of electromagnetic fields. A suitable modification of inhomogeneous environment is required so that the vacuum fluctuations controlling the SE can be manipulated. Inhibiting unwanted SEs and boosting desired ones will promote the novel optoelectronic designs tailored to industrial standards. The local density of states (LDOS) [42] counts the number of electromagnetic modes where photons can be emitted at the specific location of the emitter, and can be interpreted as the density of vacuum fluctuations. The inhibition or enhancement of SE boils down to how the LDOS of photons is controlled. The SE rate is also proportional to the LDOS. Regarding laser and light-emitting diode applications, enhancing SE enables the improved photoluminescence, low threshold current, and fast turn-on time. Meanwhile, SE can be redirected with a high directionality in the Yagi-Uda nanoantenna system, which is quite useful in the molecular detection and sensing [103]. As an efficient tool to control the SE, plasmonic effects are successfully explored to design various optical elements and devices for enhancing and redirecting the emission [82, 83]. Here, we employ the FDTD method to investigate the LDOS or SE in a hybrid plasmonic system [108] as plotted in Figure 2.12. The LDOS can be calculated by using (2.41). The localized plasmon from the nanosphere will strongly interact with the surface plasmon from the plate substrate resulting in a strong confinement and large spontaneous decay rate. Particularly,

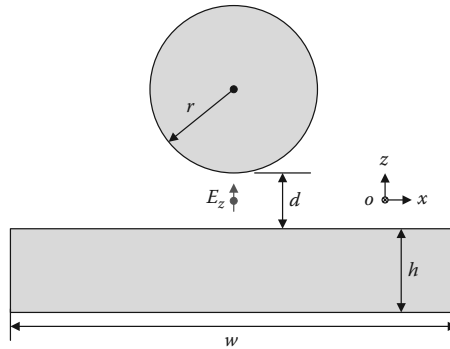


FIGURE 2.12
A schematic pattern for the SE in a hybrid plasmonic system. A gold sphere is located above the square gold substrate excited by the z-polarized dipole, where $r = 20$ nm, $d = 20$ nm, $h = 30$ nm, and $w = 100$ nm.

constructive or coherent interferences by the evanescent wave coupling in the case of z-polarized dipole make the normalized SE rate of the hybrid system stronger than the summation of those of the single nanosphere and the single substrate (Figure 2.13). Figures 2.14(a) and (b) show the scattered near-field distributions for the hybrid plasmonic system and single metallic nanosphere, respectively. The two hot spots at the opposite edges of the sphere and plate can be seen clearly in Figure 2.14(a).

2.3.4 Metamaterials

Artificially engineered metamaterials (MMs) have attracted much attention due to their interesting properties not attainable in naturally occurring

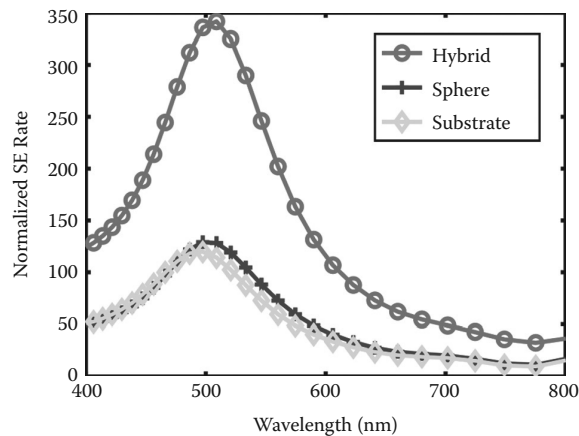


FIGURE 2.13
The normalized SE rate of a z-polarized emitter versus wavelength in a hybrid, a single sphere, and a single substrate plasmonic system.

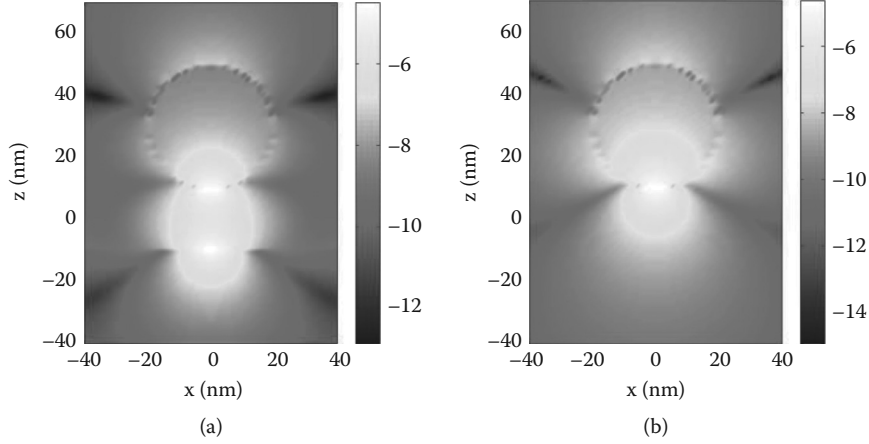


FIGURE 2.14

The scattered near-field distributions E_z of (a) a hybrid plasmonic system and (b) a single Au sphere excited with a z -polarized dipole (in the logarithmic scale). The dipole is located at $z = 0$ nm. (See color figure.)

materials, such as negative refraction, cloaking, and electromagnetically induced transparency [48–55]. Since MMs have a subwavelength scale, effective material parameters (EMPs) (involving permittivity/permeability or refractive index/impedance) [110] can be retrieved by a homogenization procedure to significantly simplify the description of MM properties. Here, the EMPs are obtained with the recently developed non-asymptotic homogenization theory [111,112], where the electromagnetic field is approximated with a suitably chosen set of basis functions (modes).

The EMPs, which can be generally represented by a 6×6 matrix, are used to describe the linear constitutive relationship of the four coarse-grained (macroscopic) electromagnetic (EM) fields $\tilde{\mathbf{E}}, \tilde{\mathbf{H}}, \tilde{\mathbf{D}}, \tilde{\mathbf{B}}$ in the frequency domain, i.e.,

$$\begin{pmatrix} \tilde{\mathbf{D}} \\ \tilde{\mathbf{B}} \end{pmatrix} = \begin{pmatrix} \{\epsilon\}_{3 \times 3} & \{\chi\}_{3 \times 3} \\ \{\xi\}_{3 \times 3} & \{\mu\}_{3 \times 3} \end{pmatrix} \begin{pmatrix} \tilde{\mathbf{E}} \\ \tilde{\mathbf{H}} \end{pmatrix} \quad (2.64)$$

The EMPs can be retrieved by inverting (2.64) with a sufficient basis set of macroscopic EM fields. In view of periodic structures, the macroscopic EM fields $\tilde{\mathbf{E}}, \tilde{\mathbf{H}}, \tilde{\mathbf{D}}, \tilde{\mathbf{B}}$ can be obtained by averaging the microscopic ones $\tilde{\mathbf{e}}, \tilde{\mathbf{h}}, \tilde{\mathbf{d}}, \tilde{\mathbf{b}}$ with the line and area integrals along the edge and surface of the unit cell of the periodic structure, respectively. Here, the FDTD method is adopted to obtain the microscopic EM fields with different excitations as basis functions [113].

An array of spherical gold particles with the radius of 20 nm in a cubic unit cell with the size of 80 nm is analyzed (see Figure 2.16[a]). The number

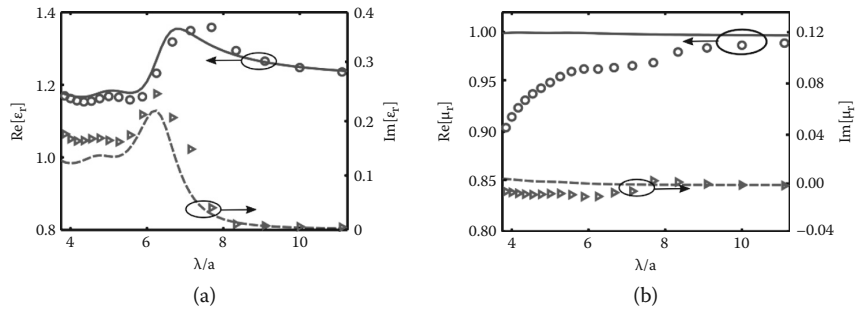


FIGURE 2.15 The diagonal elements of the EMPs for a periodic lattice of gold spheres with a radius of 20 nm and unit cell size of 80 nm. The number of lattice layers is five. (a) Relative permittivity; (b) relative permeability. Lines: the Lewin theory. Markers: Homogenized EMPs based on the FDTD simulation.

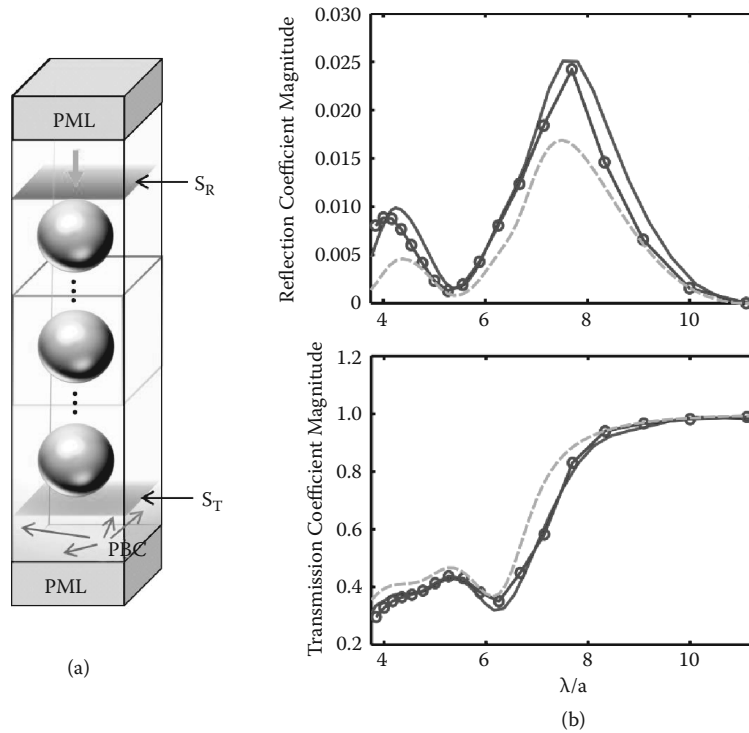


FIGURE 2.16 (a) A schematic pattern for the EMP retrieval. S_R and S_T are the planar surfaces for extracting the reflection and transmission coefficients. PML and PBC denote perfectly matched layer and periodic boundary condition, respectively. (b) The reflection and transmission coefficients. Solid red lines: real model simulation; blue circles: an equivalent slab with the EMPs obtained by the homogenization from FDTD solutions; dashed green lines: an equivalent slab with the EMPs obtained from the Lewin's theory. (See color figure.)

of lattice layers is five. The basis functions are constructed by illuminating the structure with incident waves at varying angles. PMLs are used as absorbing boundaries at the top and bottom (z -direction) of the MM slab, while PBCs are applied in the x - and y -directions. For a broadband simulation with a Gaussian pulse excitation, the constant horizontal wave number approach described in Section 2.2 is adopted especially for handling the oblique incidence case. Figure 2.15 displays the calculated EMPs compared to the Lewin's theory results [114]. Figure 2.16(b) illustrates the reflection (R) and transmission (T) coefficients used to check the validity of the EMPs. We compare the T/R coefficients calculated from the real model simulation and those calculated by an equivalent slab with the EMPs. From Figure 2.16(b), the EMPs by the homogenization from FDFD solutions are more accurate than those obtained from the Lewin's theory.

2.4 Extended to a Time-Dependent Schrödinger Equation

For conventional devices, the applied or built-in potentials vary slowly in comparison to the crystal potential, so that wave phenomena such as reflections and tunneling are absent, and therefore the electron motion can be described by classical physics. The classical approach will break down in ultra-small devices. Because most ultra-small devices contain quantum wells, the carriers within such wells clearly display their wave nature. Quantum confinements alter the wave function of electrons confined in potential wells, but the transport outside the confined region can often be described semiclassically. As a result, wave phenomena in ultra-small quantum devices, governed by the Schrödinger equation, strongly affect the device performances.

The time-dependent Schrödinger equation is given by [115]

$$i\hbar \frac{\partial \psi(\mathbf{r}, t)}{\partial t} = -\frac{\hbar^2}{2m^*} \nabla^2 \psi(\mathbf{r}, t) + V(\mathbf{r})\psi(\mathbf{r}, t) \quad (2.65)$$

where ψ is the wave function that is a probability amplitude in quantum mechanics describing the quantum state of a particle at the position r and time t , m^* is the (effective) mass of the particle, $-(\hbar^2/2m^*)\nabla^2$ is the kinetic energy operator, $V(\mathbf{r})$ is the time-independent potential energy, and $-(\hbar^2/2m^*)\nabla^2 + V$ is the Hamiltonian operator.

To avoid using complex numbers, one can separate the variable $\Psi(r, t)$ into its real and imaginary parts as

$$\Psi(r, t) = \Psi_R(r, t) + i\Psi_I(r, t) \quad (2.66)$$

Inserting (2.66) into (2.65), we get the following coupled set of equations [116,117]:

$$\hbar \frac{\partial \Psi_R(r, t)}{\partial t} = -\frac{\hbar^2}{2m^*} \left[\frac{\partial^2 \Psi_I(r, t)}{\partial x^2} + \frac{\partial^2 \Psi_I(r, t)}{\partial y^2} + \frac{\partial^2 \Psi_I(r, t)}{\partial z^2} \right] + V(r)\Psi_I(r, t) \quad (2.67)$$

$$\hbar \frac{\partial \Psi_I(r, t)}{\partial t} = \frac{\hbar^2}{2m^*} \left[\frac{\partial^2 \Psi_R(r, t)}{\partial x^2} + \frac{\partial^2 \Psi_R(r, t)}{\partial y^2} + \frac{\partial^2 \Psi_R(r, t)}{\partial z^2} \right] - V(r)\Psi_R(r, t) \quad (2.68)$$

A mesh is defined as a discrete set of grid points that sample the wave function in space and time. The discretized real and imaginary parts of the wave function can be represented as

$$\Psi_R(\mathbf{r}, t) \approx \Psi_R^n(i, j, k) = \Psi_R(i\Delta_x, j\Delta_y, k\Delta_z, n\Delta_t) \quad (2.69)$$

$$\Psi_I(\mathbf{r}, t) \approx \Psi_I^n(i, j, k) = \Psi_I(i\Delta_x, j\Delta_y, k\Delta_z, n\Delta_t) \quad (2.70)$$

where Δ_x , Δ_y , and Δ_z are, respectively, the space steps in the x -, y -, and z -directions, Δ_t is the time step, and i, j, k , and n are integers. The first-order time derivatives can be discretized by a second-order centered difference scheme. The second-order Laplace operator in (2.67) and (2.68) is discretized by using the second-order collocated difference, which distinguishes from the Yee (staggered) cell in the FDTD method for Maxwell's equations [1]. Accordingly, the update equations of the real and imaginary parts of the wave function are of the forms

$$\begin{aligned} \Psi_R^{n+1}(i, j, k) &= \Psi_R^n(i, j, k) \\ &- \frac{\hbar\Delta t}{2m^* \Delta x^2} \left[\Psi_I^{n+1/2}(i+1, j, k) - 2\Psi_I^{n+1/2}(i, j, k) + \Psi_I^{n+1/2}(i-1, j, k) \right] \\ &- \frac{\hbar\Delta t}{2m^* \Delta y^2} \left[\Psi_I^{n+1/2}(i, j+1, k) - 2\Psi_I^{n+1/2}(i, j, k) + \Psi_I^{n+1/2}(i, j-1, k) \right] \\ &- \frac{\hbar\Delta t}{2m^* \Delta z^2} \left[\Psi_I^{n+1/2}(i, j, k+1) - 2\Psi_I^{n+1/2}(i, j, k) + \Psi_I^{n+1/2}(i, j, k-1) \right] \\ &+ \frac{V(i, j, k)\Delta t}{\hbar} \times \Psi_I^{n+1/2}(i, j, k) \end{aligned} \quad (2.71)$$

$$\begin{aligned}
\Psi_i^{n+1/2}(i, j, k) = & \Psi_i^{n-1/2}(i, j, k) + \frac{\hbar\Delta t}{2m^*\Delta x^2} \left[\Psi_R^n(i+1, j, k) - 2\Psi_R^n(i, j, k) + \Psi_R^n(i-1, j, k) \right] \\
& + \frac{\hbar\Delta t}{2m^*\Delta y^2} \left[\Psi_R^n(i, j+1, k) - 2\Psi_R^n(i, j, k) + \Psi_R^n(i, j-1, k) \right] \\
& + \frac{\hbar\Delta t}{2m^*\Delta z^2} \left[\Psi_R^n(i, j, k+1) - 2\Psi_R^n(i, j, k) + \Psi_R^n(i, j, k-1) \right] \\
& - \frac{V(i, j, k)\Delta t}{\hbar} \times \Psi_R^n(i, j, k) \quad (2.72)
\end{aligned}$$

To absorb the outgoing waves, the stretched coordinate PML [118,119] is adopted. By using the case of a 1D Schrödinger equation, we have

$$i\hbar \frac{\partial \Psi(x, t)}{\partial t} = -\frac{\hbar^2}{2m^*} \left[\frac{1}{1+R\sigma(x)} \frac{\partial \Psi(x, t)}{\partial x} \left(\frac{1}{1+R\sigma(x)} \frac{\partial \Psi(x, t)}{\partial x} \right) \right] + V(\mathbf{r})\Psi(\mathbf{r}, t) \quad (2.73)$$

where $\sigma(x) = 0.005(x - x_r)^2$ is the parameter that is stretched as it approaches the edge of the problem space and $R = e^{\pi/4}$.

According to the von Neumann stability analysis, the solution of the wave function can be represented as a superposition of plane waves

$$\begin{aligned}
\Psi(x, y, z) = \Psi(i\Delta_x, j\Delta_y, k\Delta_z) = & A_0 \exp(-j_0(i\Delta_x k_x + j\Delta_y k_y + k\Delta_z k_z)) \\
k_x = k_0 \sin \theta \cos \varphi, \quad k_y = & k_0 \sin \theta \sin \varphi, \quad k_z = k_0 \cos \theta \quad (2.74)
\end{aligned}$$

where $k_x = p_m/\hbar$ is the wave number, p_m is the momentum, and θ and φ are the spherical angles. The second-order collocated differences are used to discretize the second-order spatial derivatives, i.e.,

$$\frac{\partial^2 \Psi}{\partial z^2} \approx \sum_{r=-1}^1 W_r \frac{\Psi(i, j, k+r)}{\Delta_z^2} = \sum_{r=-1}^1 W_r \frac{\exp(-j_0 r k_z \Delta_z)}{\Delta_z^2} \Psi(i, j, k) = \eta_z \Psi \quad (2.75)$$

where

$$\eta_z = \sum_{r=-1}^1 W_r \frac{\exp(-j_0 r k_z \Delta_z)}{\Delta_z^2} \quad \text{and} \quad W = \{1, -2, 1\}.$$

For simplicity, we consider a 1D Schrödinger equation with zero potential energy

$$\frac{\partial}{\partial t} \begin{pmatrix} \Psi_R \\ \Psi_I \end{pmatrix} = \begin{pmatrix} 0 & -\frac{\hbar}{2m^*} \frac{\partial^2}{\partial z^2} \\ \frac{\hbar}{2m^*} \frac{\partial^2}{\partial z^2} & 0 \end{pmatrix} \begin{pmatrix} \Psi_R \\ \Psi_I \end{pmatrix} \quad (2.76)$$

and corresponding spatial discretization form is given by

$$\frac{\partial}{\partial t} \begin{pmatrix} \Psi_R \\ \Psi_I \end{pmatrix} = \begin{pmatrix} 0 & -\frac{\hbar}{2m^*} \eta_z \\ \frac{\hbar}{2m^*} \eta_z & 0 \end{pmatrix} \begin{pmatrix} \Psi_R \\ \Psi_I \end{pmatrix} \quad (2.77)$$

It is trivial to access the discretized evolution matrix L^d with the second-order staggered time-stepping method

$$L^d = \begin{bmatrix} l_{11} & l_{12} \\ l_{21} & l_{22} \end{bmatrix} = \prod_{l=1}^m \begin{pmatrix} 1 & 0 \\ \frac{\hbar}{2m^*} \eta_z d_l \Delta_t & 1 \end{pmatrix} \begin{pmatrix} 1 & -\frac{\hbar}{2m^*} \eta_z c_l \Delta_t \\ 0 & 1 \end{pmatrix} \quad (2.78)$$

where $m = 2$, $c_1 = c_2 = 0.5$, $d_1 = 1$, and $d_2 = 0$.

The eigenvalues λ of the discretized evolution matrix satisfy the following eigen-equation

$$\lambda^2 - \text{tr}(L^d)\lambda + \det(L^d) = 0 \quad (2.79)$$

where $\text{tr}(L^d)$ and $\det(L^d)$ are the trace and determinant of the evolution matrix, respectively. Considering that the determinant of the discretized evolution matrix is 1, the eigen-equation can be simplified as

$$\lambda^2 - \text{tr}(L^d)\lambda + 1 = 0 \quad (2.80)$$

and its solutions are

$$\lambda_{1,2} = \frac{\text{tr}(L^d) \pm j_0 \sqrt{4 - [\text{tr}(L^d)]^2}}{2}$$

A stable algorithm requires $|\lambda_{1,2}| = 1$, and thus $|\text{tr}(L^d)| \leq 2$. Through terms of matrix multiplications, we have

$$\text{tr}(L^d) = 2 + \sum_{l=1}^m (-1)^l g_l \left(\left(\frac{\hbar}{2m^*} \right)^2 \Delta_t^2 \eta_z^2 \right)^l \quad (2.81)$$

$$g_l = \sum_{1 \leq i_1 \leq j_1 < i_2 \leq j_2 < \dots < i_l \leq j_l \leq m} c_{i_1} d_{j_1} c_{i_2} d_{j_2} \dots c_{i_l} d_{j_l} + \sum_{1 \leq i_1 < j_1 \leq i_2 < j_2 \leq \dots \leq i_l < j_l \leq m} d_{i_1} c_{j_1} d_{i_2} c_{j_2} \dots d_{i_l} c_{j_l} \quad (2.82)$$

The above results can be generalized to a three-dimensional (3D) Schrödinger equation with zero potential energy, i.e.,

$$\text{tr}(L^d) = 2 + \sum_{l=1}^m (-1)^l g_l \left(\left(\frac{\hbar}{2m^*} \right)^2 \Delta_r^2 (\eta_x + \eta_y + \eta_z)^2 \right)^l \quad (2.83)$$

Finally, we can get

$$\sqrt{\frac{\hbar}{m^*} \frac{\Delta_r}{\Delta_s^2}} \leq CFL \quad (2.84)$$

where $CFL = 1/\sqrt{d}$ is the Courant-Friedrichs-Levy (CFL) number and $d = 1, 2, 3$ is the dimension number.

The dispersion relation of free space photon described by Maxwell's equations is

$$\omega = c |\mathbf{k}_0| \quad (2.85)$$

where c is the speed of light and $\mathbf{k}_0 = (k_x, k_y, k_z)$ is the wave vector with the amplitude of k_0 . Critically different from free space photon with the cone-shaped dispersion relation, the dispersion relation of free electron is a paraboloid, i.e.,

$$\omega = \left(\frac{\hbar}{2m^*} \right) |\mathbf{k}_0|^2 \quad (2.86)$$

We can define a dummy velocity of the Schrödinger equation as $v_0 = (\hbar/2m^*)$, analogous to Maxwell's equations, so (2.86) can be rewritten as

$$\omega = v_0 |\mathbf{k}_0|^2 \quad (2.87)$$

Due to the energy-conserving property of the second-order staggered time-stepping method, the dispersion relation of free electron can be written as

$$\omega \Delta_t = a \cos \left[\frac{\text{tr}(L^d)}{2} \right] \quad (2.88)$$

The relative error of phase velocity is given by

$$\eta = \left| \frac{v_p - v_0}{v_0} \right| \quad (2.89)$$

where $v_p = \omega/k_0^2$, and ω can be obtained by (2.88). The above analyses for the numerical stability and dispersion can be extended to the high-order quantum FDTD approaches [120].

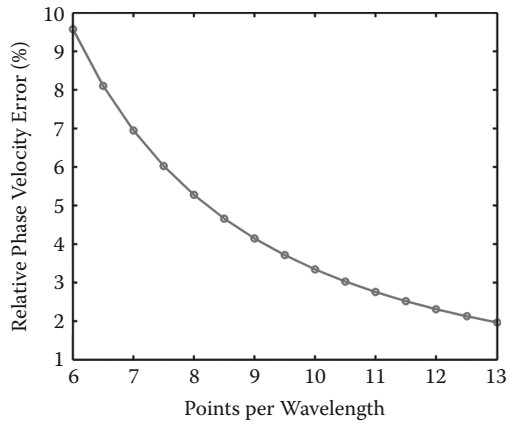


FIGURE 2.17 The relative dispersion error as a function of the spatial resolution (points per wavelength). Here, the spherical angles are set to $\theta = 0^\circ$, $\varphi = 0^\circ$, and the stability constant is $S_\delta = \frac{\Delta_t}{\Delta_\delta^2} \frac{\hbar}{2m^*} = 0.125$.

We set the stability criterion to be

$$S_\delta = \frac{\Delta_t}{\Delta_\delta^2} \frac{\hbar}{2m^*} = 0.125$$

Figure 2.17 shows the relative phase velocity error as a function of points per wavelength (PPW) for a plane wave traveling at $\theta = 0^\circ$ and $\varphi = 0^\circ$. Next, the spatial resolution is set to be 7 points per wavelength. We redraw the relative error at $\theta = 30^\circ$ versus the propagating angle φ as shown in Figure 2.18.

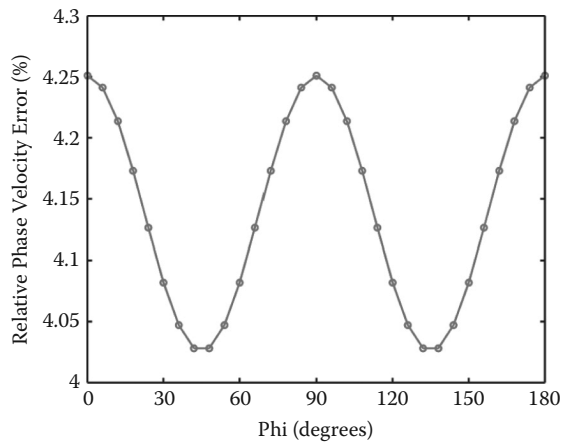


FIGURE 2.18 The relative dispersion error as a function of the spherical angle φ . The spherical angle is $\theta = 30^\circ$, the spatial resolution is 7 points per wavelength, and the stability constant is $S_\delta = \frac{\Delta_t}{\Delta_\delta^2} \frac{\hbar}{2m^*} = 0.125$.

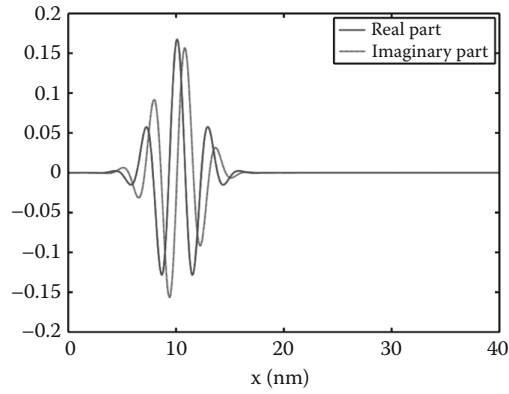
2.5 Numerical Examples for Quantum Physics

2.5.1 1D Propagation Problem

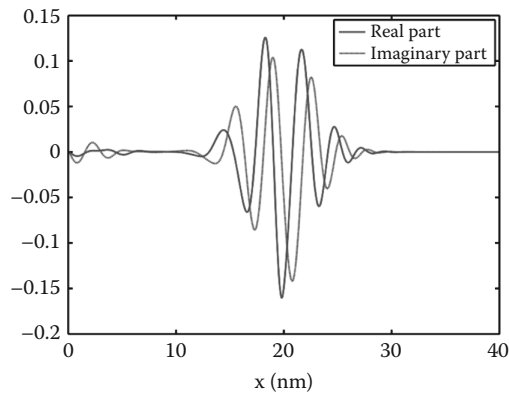
We consider a simulation of a particle interacting with a barrier of 0.1 eV. The spatial step is $\Delta_s = 0.1$ nm and

$$S_\delta = \frac{\Delta_t}{\Delta_s^2} \frac{\hbar}{2m^*} = 0.1$$

The simulation domain occupies 400 grids. Figure 2.19 shows the propagation of the particle near the barrier with the initial wave function of a modulated



(a) 0 fs



(b) 40 fs

FIGURE 2.19

A particle is initiated in free space and strikes a barrier with a potential of 0.1 eV. The time evolutions of the wave function are recorded. (*Continued*)

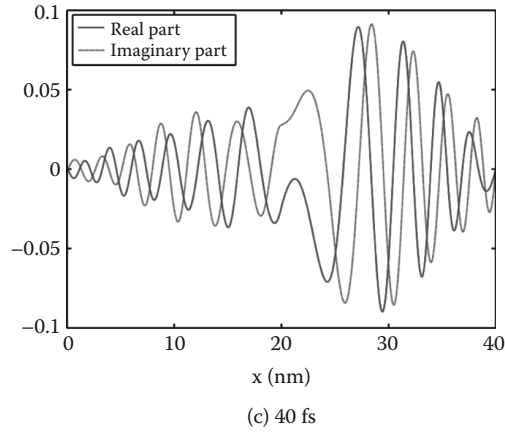


FIGURE 2.19 (Continued)

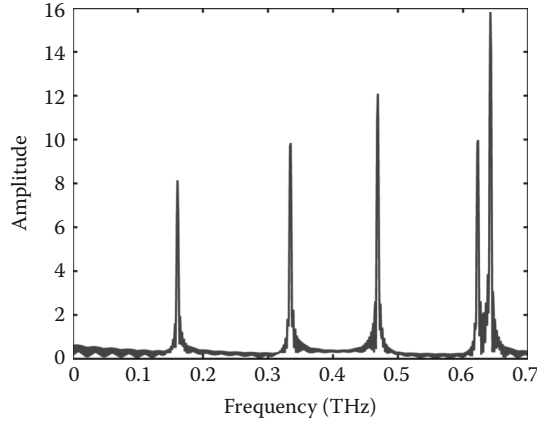
A particle is initiated in free space and strikes a barrier with a potential of 0.1 eV. The time evolutions of the wave function are recorded.

Gaussian pulse. After 40 fs, the particle reaches the barrier. After 90 fs, the wave function is reflected back and meanwhile penetrated into the barrier.

2.5.2 Two-Dimensional Eigenvalue Problem

The eigenvalue problem of the Schrödinger equation is fundamentally important for the quantum transport and nanodevice modeling. The ballistic electron transport strongly depends on the transverse eigenstates of the conducting channel [121]. Various intriguing quantum phenomena for the microscopic electron transport, such as the resonant tunneling effect [115], Fano-resonance [122], and so on, contribute to the excitation of eigenstates or interplay of different eigenstates. Thus, an accurate and efficient method to calculate the eigenstates and eigenfrequencies is crucial to understand the fundamental and device physics. Moreover, eigenstates and eigenfrequencies extraction tailored to industrial requirements is also indispensable in the quantum computer-aided design (CAD). One of the commonly adopted algorithms to solve the eigenvalue problem of the time-dependent Schrödinger equation is the FDTD method [116,117]. Here we investigate the eigenvalue problem of a particle in a two-dimensional (2D) quantum well with the area of $40 \times 30 \text{ nm}^2$. The spatial steps are set to $\Delta_x = \Delta_y = 1 \text{ nm}$, and

$$S_{\delta} = \frac{\Delta_t}{\Delta_{\delta}^2} \frac{\hbar}{2m^*} = 0.1$$

**FIGURE 2.20**

The eigenfrequencies of a 2D quantum well calculated by the quantum FDTD method and discrete (fast) Fourier transform.

The simulation time step is set to 200,000 to force all the eigenstates completely excited. The initial value of the wave function is taken as (2.42). Figure 2.20 shows the amplitude-frequency spectrum at an arbitrary point of the quantum well from 0 to 0.7 THz calculated by the quantum FDTD method and discrete (fast) Fourier transform. Table 2.1 lists the eigenfrequencies related to the amplitude peaks in Figure 2.20. The calculated eigenfrequencies by the quantum FDTD method agree with the analytical solutions well. The eigenstate corresponding to one of the eigenfrequencies is illustrated in Figure 2.21.

TABLE 2.1

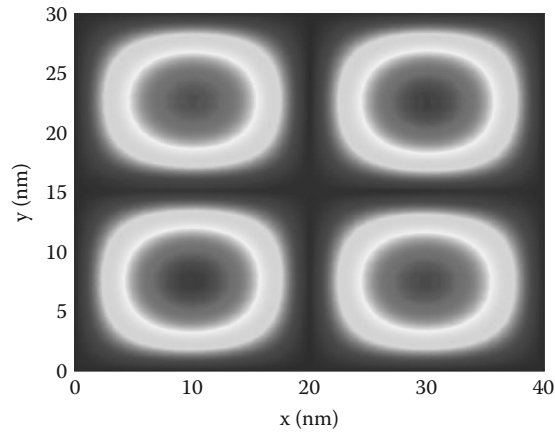
Comparisons of Eigenfrequencies of a 2D Quantum Well between the FDTD Method and the Analytical Solution

Eigenfrequencies	Numerical (THz)	Analytical (THz)
f_{11}	0.161	0.158
f_{21}	0.335	0.328
f_{12}	0.469	0.461
f_{31}	0.623	0.613
f_{22}	0.642	0.631

Note: The analytical solution is

$$f_{pq} = \frac{\hbar\pi}{4m^*} \left(\frac{p^2}{a^2} + \frac{q^2}{b^2} \right),$$

where p, q are integers, and a and b are the length and width of the well.

**FIGURE 2.21**

The eigenstate corresponding to the eigenfrequency f_{22} for a 2D quantum well obtained by the quantum FDTD method and discrete Fourier transform. (See color figure.)

2.6 Conclusion

The FDTD method and its advances tremendously promote the development of the computational electromagnetics field and play more and more fundamental roles in nanotechnology applications. Due to the features of extreme flexibility and easy implementation, the FDTD method is an indispensable tool in modeling inhomogeneous, anisotropic, and dispersive media with random, multilayered, and periodic fundamental (or device) nanostructures. Regarding future possible research directions, the FDTD method is expected to be widely adopted to simulate multiphysics problems, through which the optical, electrical, thermal, mechanical, and quantum properties of multifunctional components and devices can be investigated. Based on authors' knowledge, some interesting and hot topics for the multiphysics simulation are summarized as follows:

1. Nonlinear optics problem, such as the second harmonic generation, Kerr effect, and four-wave mixing [123]. The Maxwell's equations and hydrodynamic equation can be solved self-consistently [124].
2. Optoelectronic device simulation for light-emitting diodes, photo-detectors, solar cells, and lasers. The Maxwell's equations, semiconductor equations (Poisson, drift-diffusion, continuity, heat conduction, and energy balance equations), and thermal stress field equations will be coupled with each other [125–127]. The Maxwell's equations also could be interacted with the rate equations [128,129].

3. Quantum optics and quantum transport problems. The self-consistent solutions to Maxwell's equations and effective-mass Schrödinger equation, von Neumann equation, or density functional theory method are required [130,131].

Exploring start-of-the-art techniques and emerging applications for the FDTD method will open up a fantastic, fruitful, and challenging research area in the near future. Are you ready?

Acknowledgment

The authors acknowledge the support of the grants from the National Natural Science Foundation of China (No. 61201122 and No. 60931002).

References

1. K. S. Yee, "Numerical solution of initial boundary value problems involving Maxwell's equations in isotropic media," *IEEE Trans. Antennas Propag.* 14, 302–307 (1966).
2. A. Taflove, *Computational Electrodynamics: The Finite-Difference Time-Domain Method*. Norwood, MA: Artech House, 1995.
3. A. Taflove, et al., *Advances in Computational Electrodynamics: The Finite-Difference Time-Domain Method*. Norwood, MA: Artech House, 1998.
4. D. M. Sullivan, *Electromagnetic Simulation Using the FDTD Method*. New York: IEEE Press, 2000.
5. J. L. Young, D. Gaitonde, and J. S. Shang, "Toward the construction of a fourth-order difference scheme for transient EM wave simulation: Staggered grid approach," *IEEE Trans. Antennas Propag.* 45, 1573–1580 (1997).
6. J. S. Shang, "High-order compact-difference schemes for time-dependent Maxwell equations," *J. Comput. Phys.* 153, 312–333 (1999).
7. T. Namiki, "New FDTD algorithm based on alternating-direction implicit method," *IEEE Trans. Microw. Theory Tech.* 47, 2003–2007 (1999).
8. F. H. Zhen, Z. Z. Chen, and J. Z. Zhang, "Toward the development of a three-dimensional unconditionally stable finite-difference time-domain method," *IEEE Trans. Microw. Theory Tech.* 48, 1550–1558 (2000).
9. J. S. Kole, M. T. Figge, and H. De Raedt, "Higher-order unconditionally stable algorithms to solve the time-dependent Maxwell equations," *Phys. Rev. E* 65, 066705 (2002).
10. G. Sun and C. W. Trueman, "Unconditionally stable Crank-Nicolson scheme for solving two-dimensional Maxwell's equations," *Electron. Lett.* 39, 595–597 (2003).

11. J. Shibayama, M. Muraki, J. Yamauchi, and H. Nakano, "Efficient implicit FDTD algorithm based on locally one-dimensional scheme," *Electron. Lett.* 41, 1046–1047 (2005).
12. H. Yoshida, "Construction of higher order symplectic integrators," *Physica D* 46, 262–268 (1990).
13. T. Hirono, W. Lui, S. Seki, and Y. Yoshikuni, "A three-dimensional fourth-order finite-difference time-domain scheme using a symplectic integrator propagator," *IEEE Trans. Microw. Theory Tech.* 49, 1640–1648 (2001).
14. W. E. I. Sha, Z. X. Huang, X. L. Wu, and M. S. Chen, "Application of the symplectic finite-difference time-domain scheme to electromagnetic simulation," *J. Comput. Phys.* 225, 33–50 (2007).
15. W. E. I. Sha, Z. X. Huang, M. S. Chen, and X. L. Wu, "Survey on symplectic finite-difference time-domain schemes for Maxwell's equations," *IEEE Trans. Antennas Propag.* 56, 493–500 (2008).
16. M. Okoniewski, E. Okoniewska, and M. A. Stuchly, "Three-dimensional subgridding algorithm for FDTD," *IEEE Trans. Antennas Propag.* 45, 422–429 (1997).
17. S. Dey and R. Mittra, "A locally conformal finite-difference time-domain algorithm for modeling three-dimensional perfectly conducting objects," *IEEE Microwave and Guided Wave Letters* 7, 273–275 (1997).
18. T. G. Jurgens, A. Taflove, K. Umashankar, and T. G. Moore, "Finite-difference time-domain modeling of curved surfaces," *IEEE Trans. Antennas Propag.* 40, 357–366 (1992).
19. W. H. Yu and R. Mittra, "A conformal FDTD algorithm for modeling perfectly conducting objects with curve-shaped surfaces and edges," *Microw. Opt. Technol. Lett.* 27, 136–138 (2000).
20. I. A. Zagorodnov, R. Schuhmann, and T. Weiland, "A uniformly stable conformal FDTD-method in Cartesian grids," *Int. J. Numer. Model.-Electron. Netw. Device Fields* 16, 127–141 (2003).
21. T. Xiao and Q. H. Liu, "Enlarged cells for the conformal FDTD method to avoid the time step reduction," *IEEE Microw. Wirel. Compon. Lett.* 14, 551–553 (2004).
22. J. Fang, "Time domain finite difference computation for Maxwell's equations," Ph.D. dissertation, Univ. California, Berkeley, CA, 1989.
23. A. Yefet and P. G. Petropoulos, "A staggered fourth-order accurate explicit finite difference scheme for the time-domain Maxwell's equations," *J. Comput. Phys.* 168, 286–315 (2001).
24. S. V. Georgakopoulos, C. R. Birtcher, C. A. Balanis, and R. A. Renaut, "Higher-order finite-difference schemes for electromagnetic radiation, scattering, and penetration, Part I: Theory," *IEEE Antennas Propag. Mag.* 44, 134–142 (2002).
25. S. V. Georgakopoulos, C. R. Birtcher, C. A. Balanis, and R. A. Renaut, "Higher-order finite-difference schemes for electromagnetic radiation, scattering, and penetration, Part 2: Applications," *IEEE Antennas Propag. Mag.* 44, 92–101 (2002).
26. W. E. I. Sha, X. L. Wu, M. S. Chen, and Z. X. Huang, "Application of the high-order symplectic FDTD scheme to the curved three-dimensional perfectly conducting objects," *Microw. Opt. Technol. Lett.* 49, 931–934 (2007).
27. W. E. I. Sha, X. L. Wu, Z. X. Huang, and M. S. Chen, "A new conformal FDTD(2,4) scheme for modeling three-dimensional curved perfectly conducting objects," *IEEE Microw. Wirel. Compon. Lett.* 18, 149–151 (2008).

28. J. A. Wang, W. Y. Yin, P. G. Liu, and Q. H. Liu, "High-order interface treatment techniques for modeling curved dielectric objects," *IEEE Trans. Antennas Propag.* 58, 2946–2953 (2010).
29. B. A. Al-Zohouri and M. F. Hadi, "Conformal modelling of perfect conductors in the high-order M24 finite-difference time-domain algorithm," *IET Microw. Antennas Propag.* 5, 583–587 (2011).
30. M. Krumpholz and L. P. B. Katehi, "MRTD: New time-domain schemes based on multiresolution analysis," *IEEE Trans. Microw. Theory Tech.* 44, 555–571 (1996).
31. Q. S. Cao, Y. C. Chen, and R. Mittra, "Multiple image technique (MIT) and anisotropic perfectly matched layer (APML) in implementation of MRTD scheme for boundary truncations of microwave structures," *IEEE Trans. Microw. Theory Tech.* 50, 1578–1589 (2002).
32. Q. H. Liu, "PSTD algorithm: A time-domain method requiring only two cells per wavelength," *Microw. Opt. Technol. Lett.* 15, 158–165 (1997).
33. F. Edelvik and G. Ledfelt, "A comparison of time-domain hybrid solvers for complex scattering problems," *Int. J. Numer. Model.-Electron. Netw. Device Fields* 15, 475–487 (2002).
34. A. Monorchio, A. R. Bretones, R. Mittra, G. Manara, and R. G. Martin, "A hybrid time-domain technique that combines the finite element, finite difference and method of moment techniques to solve complex electromagnetic problems," *IEEE Trans. Antennas Propag.* 52, 2666–2674 (2004).
35. T. Rylander and A. Bondeson, "Stable FEM-FDTD hybrid method for Maxwell's equations," *Comput. Phys. Commun.* 125, 75–82 (2000).
36. J. F. Lee, R. Lee, and A. Cangellaris, "Time-domain finite-element methods," *IEEE Trans. Antennas Propag.* 45, 430–442 (1997).
37. V. Shankar, A. H. Mohammadian, and W. F. Hall, "A time-domain, finite-volume treatment for the Maxwell equations," *Electromagnetics* 10, 127–145 (1990).
38. J. S. Hesthaven and T. Warburton, "Nodal high-order methods on unstructured grids—I. Time-domain solution of Maxwell's equations," *J. Comput. Phys.* 181, 186–221 (2002).
39. K. Sakoda, *Optical Properties of Photonic Crystals*. Berlin: Springer, 2005.
40. J. D. Joannopoulos, S. G. Johnson, J. N. Winn, and R. D. Meade, *Photonic Crystals Molding the Flow of Light*. Woodstock: Princeton University Press, 2008.
41. W. L. Barnes, A. Dereux, and T. W. Ebbesen, "Surface plasmon subwavelength optics," *Nature* 424, 824–830 (2003).
42. L. Novotny, and B. Hecht, *Principles of Nano-Optics*. Cambridge University Press, 2006.
43. S. Kawata, and V. M. Shalaev, *Nanophotonics with Surface Plasmons*. Elsevier, 2007.
44. S. A. Maier, *Plasmonics: Fundamentals and Applications*. Springer, 2007.
45. H. A. Atwater, and A. Polman, "Plasmonics for improved photovoltaic devices," *Nat. Mater.* 9, 205–213 (2010).
46. D. K. Gramotnev, and S. I. Bozhevolnyi, "Plasmonics beyond the diffraction limit," *Nat. Photonics* 4, 83–91 (2010).
47. J. A. Schuller, E. S. Barnard, W. S. Cai, Y. C. Jun, J. S. White, and M. L. Brongersma, "Plasmonics for extreme light concentration and manipulation," *Nat. Mater.* 9, 193–204 (2010).

48. J. B. Pendry, A. J. Holden, D. J. Robbins, and W. J. Stewart, "Magnetism from conductors and enhanced nonlinear phenomena," *IEEE Trans. Microw. Theory Tech.* 47, 2075–2084 (1999).
49. J. B. Pendry, "Negative refraction makes a perfect lens," *Phys. Rev. Lett.* 85, 3966–3969 (2000).
50. D. R. Smith, W. J. Padilla, D. C. Vier, S. C. Nemat-Nasser, and S. Schultz, "Composite medium with simultaneously negative permeability and permittivity," *Phys. Rev. Lett.* 84, 4184–4187 (2000).
51. D. R. Smith, J. B. Pendry, and M. C. K. Wiltshire, "Metamaterials and negative refractive index," *Science* 305, 788–792 (2004).
52. V. M. Shalaev, W. S. Cai, U. K. Chettiar, H. K. Yuan, A. K. Sarychev, V. P. Drachev, and A. V. Kildishev, "Negative index of refraction in optical metamaterials," *Opt. Lett.* 30, 3356–3358 (2005).
53. N. Engheta and R. W. Ziolkowski, *Metamaterials: Physics and Engineering Explorations*. Wiley-IEEE Press, 2006.
54. V. M. Shalaev, "Optical negative-index metamaterials," *Nat. Photonics* 1, 41–48 (2007).
55. C. M. Soukoulis and M. Wegener, "Past achievements and future challenges in the development of three-dimensional photonic metamaterials," *Nat. Photonics* 5, 523–530 (2011).
56. J. P. Berenger, "Three-dimensional perfectly matched layer for the absorption of electromagnetic waves," *J. Comput. Phys.* 127, 363–379 (1996).
57. S. D. Gedney, "An anisotropic PML absorbing media for the FDTD simulation of fields in lossy and dispersive media," *Electromagnetics* 16, 399–415 (1996).
58. J. A. Roden and S. D. Gedney, "Convolution PML (CPML): An efficient FDTD implementation of the CFS-PML for arbitrary media," *Microw. Opt. Technol. Lett.* 27, 334–339 (2000).
59. M. Francardi, L. Balet, A. Gerardino, N. Chauvin, D. Bitauld, L. H. Li, B. Alloing, and A. Fiore, "Enhanced spontaneous emission in a photonic-crystal light-emitting diode," *Appl. Phys. Lett.* 93, 143102 (2008).
60. M. A. Noginov, H. Li, Y. A. Barnakov, D. Dryden, G. Nataraj, G. Zhu, C. E. Bonner, M. Mayy, Z. Jacob, and E. E. Narimanov, "Controlling spontaneous emission with metamaterials," *Opt. Lett.* 35, 1863–1865 (2010).
61. C. Walther, G. Scalari, M. I. Amanti, M. Beck, and J. Faist, "Microcavity laser oscillating in a circuit-based resonator," *Science* 327, 1495–1497 (2010).
62. P. F. Qiao, W. E. I. Sha, W. C. H. Choy, and W. C. Chew, "Systematic study of spontaneous emission in a two-dimensional arbitrary inhomogeneous environment," *Phys. Rev. A* 83, 043824 (2011).
63. J. J. Greffet, R. Carminati, K. Joulain, J. P. Mulet, S. P. Mainguy, and Y. Chen, "Coherent emission of light by thermal sources," *Nature* 416, 61–64 (2002).
64. K. Joulain, J. P. Mulet, F. Marquier, R. Carminati, and J. J. Greffet, "Surface electromagnetic waves thermally excited: Radiative heat transfer, coherence properties and Casimir forces revisited in the near field," *Surf. Sci. Rep.* 57, 59–112 (2005).
65. Y. De Wilde, F. Formanek, R. Carminati, B. Gralak, P. A. Lemoine, K. Joulain, J. P. Mulet, Y. Chen, and J. J. Greffet, "Thermal radiation scanning tunnelling microscopy," *Nature* 444, 740–743 (2006).
66. L. D. Landau, E. M. Lifshitz, and L. P. Pitaevskii, *Statistical Physics. Part 2*. New York: Pergamon, 1980.

67. J. L. Xiong and W. C. Chew, "Efficient evaluation of Casimir force in z-invariant geometries by integral equation methods," *Appl. Phys. Lett.* 95, 154102 (2009).
68. P. R. Atkins, W. C. Chew, Q. I. Dai, and W. E. I. Sha, "The Casimir force for arbitrary three-dimensional objects with low frequency methods," *Progress In Electromagnetics Research Symposium*, 738–741 (2012).
69. D. M. Callahan, J. N. Munday, and H. A. Atwater, "Solar cell light trapping beyond the ray optic limit," *Nano Lett.* 12, 214–218 (2012).
70. A. F. Oskooi, D. Roundy, M. Ibanescu, P. Bermel, J. D. Joannopoulos, and S. G. Johnson, "MEEP: A flexible free-software package for electromagnetic simulations by the FDTD method," *Comput. Phys. Commun.* 181, 687–702 (2010).
71. S. M. Rao, *Time Domain Electromagnetics*. New York: Academic Press, 1999.
72. L. Novotny and N. van Hulst, "Antennas for light," *Nat. Photonics* 5, 83–90 (2011).
73. A. Yariv, Y. Xu, R. K. Lee, and A. Scherer, "Coupled-resonator optical waveguide: A proposal and analysis," *Opt. Lett.* 24, 711–713 (1999).
74. T. Kawanishi and M. Izutsu, "Coaxial periodic optical waveguide," *Opt. Express* 7, 10–22 (2000).
75. A. Alu and N. Engheta, "Tuning the scattering response of optical nanoantennas with nanocircuit loads," *Nat. Photonics* 2, 307–310 (2008).
76. H. Ichikawa and T. Baba, "Efficiency enhancement in a light-emitting diode with a two-dimensional surface grating photonic crystal," *Appl. Phys. Lett.* 84, 457–459 (2004).
77. M. C. Y. Huang, Y. Zhou, and C. J. Chang-Hasnain, "A surface-emitting laser incorporating a high-index-contrast subwavelength grating," *Nat. Photonics* 1, 119–122 (2007).
78. W. E. I. Sha, W. C. H. Choy, and W. C. Chew, "A comprehensive study for the plasmonic thin-film solar cell with periodic structure," *Opt. Express* 18, 5993–6007 (2010).
79. W. E. I. Sha, W. C. H. Choy, and W. C. Chew, "Angular response of thin-film organic solar cells with periodic metal back nanostrips," *Opt. Lett.* 36, 478–480 (2011).
80. Y. A. Vlasov, M. O'Boyle, H. F. Hamann, and S. J. McNab, "Active control of slow light on a chip with photonic crystal waveguides," *Nature* 438, 65–69 (2005).
81. T. Baba, "Slow light in photonic crystals," *Nat. Photonics* 2, 465–473 (2008).
82. H. Aouani, O. Mahboub, E. Devaux, H. Rigneault, T. W. Ebbesen, and J. Wenger, "Plasmonic antennas for directional sorting of fluorescence emission," *Nano Lett.* 11, 2400–2406 (2011).
83. Y. C. Jun, K. C. Y. Huang, and M. L. Brongersma, "Plasmonic beaming and active control over fluorescent emission," *Nat. Commun.* 2, 283 (2011).
84. A. Hessel and A. A. Oliner, "A new theory of Wood's anomalies on optical gratings," *Appl. Optics* 4, 1275–1297 (1965).
85. B. Luk'yanchuk, N. I. Zheludev, S. A. Maier, N. J. Halas, P. Nordlander, H. Giessen, and C. T. Chong, "The Fano resonance in plasmonic nanostructures and metamaterials," *Nat. Mater.* 9, 707–715 (2010).
86. A. E. Miroshnichenko, S. Flach, and Y. S. Kivshar, "Fano resonances in nanoscale structures," *Rev. Mod. Phys.* 82, 2257–2298 (2010).
87. M. D. Lukin and A. Imamoglu, "Controlling photons using electromagnetically induced transparency," *Nature* 413, 273–276 (2001).

88. K. ElMahgoub, F. Yang, and A. Elsherbeni, *Scattering Analysis of Periodic Structures Using Finite-Difference Time-Domain Method*. Morgan & Claypool Publishers, 2012.
89. R. Luebbers, F. P. Hunsberger, K. S. Kunz, R. B. Standler, and M. Schneider, "A frequency-dependent finite-difference time-domain formulation for dispersive materials," *IEEE Trans. Electromagn. Compat.* 32, 222–227 (1990).
90. T. Kashiwa and I. Fukai, "A treatment by the FD-TD method of the dispersive characteristics associated with electronic polarization," *Microw. Opt. Technol. Lett.* 3, 203–205 (1990).
91. D. F. Kelley and R. J. Luebbers, "Piecewise linear recursive convolution for dispersive media using FDTD," *IEEE Trans. Antennas Propag.* 44, 792–797 (1996).
92. D. M. Sullivan, "Frequency-dependent FDTD methods using z-transforms," *IEEE Trans. Antennas Propag.* 40, 1223–1230 (1992).
93. J. Nelson, *The Physics of Solar Cells*. London: Imperial College Press, 2003.
94. K. L. Chopra, P. D. Paulson, and V. Dutta, "Thin-film solar cells: An overview," *Prog. Photovoltaics* 12, 69–92 (2004).
95. A. D. Rakic, A. B. Djuricic, J. M. Elazar, and M. L. Majewski, "Optical properties of metallic films for vertical-cavity optoelectronic devices," *Appl. Optics* 37, 5271–5283 (1998).
96. E. D. Palik, *Handbook of Optical Constants of Solids*. London: Academic Press, 1998.
97. M. G. Moharam, E. B. Grann, D. A. Pommet, and T. K. Gaylord, "Formulation for stable and efficient implementation of the rigorous coupled-wave analysis of binary gratings," *J. Opt. Soc. Am. A* 12, 1068–1076 (1995).
98. P. Muhlschlegel, H. J. Eisler, O. J. F. Martin, B. Hecht, and D. W. Pohl, "Resonant optical antennas," *Science* 308, 1607–1609 (2005).
99. J. J. Li, A. Salandrino, and N. Engheta, "Shaping light beams in the nanometer scale: A Yagi-Uda nanoantenna in the optical domain," *Phys. Rev. B* 76, 245403 (2007).
100. T. H. Taminiau, F. D. Stefani, and N. F. van Hulst, "Enhanced directional excitation and emission of single emitters by a nano-optical Yagi-Uda antenna," *Opt. Express* 16, 10858–10866 (2008).
101. A. Kinkhabwala, Z. F. Yu, S. H. Fan, Y. Avlasevich, K. Mullen, and W. E. Moerner, "Large single-molecule fluorescence enhancements produced by a bowtie nanoantenna," *Nat. Photonics* 3, 654–657 (2009).
102. Y. G. Liu, Y. Li, and W. E. I. Sha, "Directional far-field response of a spherical nanoantenna," *Opt. Lett.* 36, 2146–2148 (2011).
103. Y. G. Liu, W. C. H. Choy, W. E. I. Sha, and W. C. Chew, "Unidirectional and wavelength-selective photonic sphere-array nanoantennas," *Opt. Lett.* 37, 2112–2114 (2012).
104. T. Kalkbrenner, U. Hakanson, A. Schadle, S. Burger, C. Henkel, and V. Sandoghdar, "Optical microscopy via spectral modifications of a nanoantenna," *Phys. Rev. Lett.* 95, 200801 (2005).
105. J. Grand, M. L. de la Chapelle, J. L. Bijeon, P. M. Adam, A. Vial, and P. Royer, "Role of localized surface plasmons in surface-enhanced Raman scattering of shape-controlled metallic particles in regular arrays," *Phys. Rev. B* 72, 033407 (2005).
106. W. E. I. Sha, W. C. H. Choy, Y. P. Chen, and W. C. Chew, "Optical design of organic solar cell with hybrid plasmonic system," *Opt. Express* 19, 15908–15918 (2011).

107. W. E. I. Sha, W. C. H. Choy, Y. G. Liu, and W. C. Chew, "Near-field multiple scattering effects of plasmonic nanospheres embedded into thin-film organic solar cells," *Appl. Phys. Lett.* 99, 113304 (2011).
108. Y. P. Chen, W. E. I. Sha, W. C. H. Choy, L. J. Jiang, and W. C. Chew, "Study on spontaneous emission in complex multilayered plasmonic system via surface integral equation approach with layered medium Green's function," *Opt. Express* 20, 20210–20221 (2012).
109. E. M. Purcell, "Spontaneous emission probabilities at radio frequencies," *Phys. Rev. Lett.* 69, 681 (1946).
110. D. R. Smith, S. Schultz, P. Markos, and C. M. Soukoulis, "Determination of effective permittivity and permeability of metamaterials from reflection and transmission coefficients," *Phys. Rev. B* 65, 195104 (2002).
111. A. Pors, I. Tsukerman, and S. I. Bozhevolnyi, "Effective constitutive parameters of plasmonic metamaterials: Homogenization by dual field interpolation," *Phys. Rev. E* 84, 016609 (2011).
112. I. Tsukerman, "Effective parameters of metamaterials: a rigorous homogenization theory via Whitney interpolation," *J. Opt. Soc. Am. B* 28, 577–586 (2011).
113. X. Y. Z. Xiong, L. J. Jiang, V. A. Markel, and I. Tsukerman, "Surface waves in three-dimensional electromagnetic composites and their effect on homogenization," *Opt. Express* 21, 10412–10421 (2013).
114. L. Lewin, "The electrical constants of a material loaded with spherical particles," *Journal of the Institution of Electrical Engineers* 94, 65–68 (1947).
115. D. J. Griffiths, *Introduction to Quantum Mechanics*, 2nd ed. Boston: Addison-Wesley, 2004.
116. A. Soriano, E. A. Navarro, J. A. Porti, and V. Such, "Analysis of the finite difference time domain technique to solve the Schrodinger equation for quantum devices," *J. Appl. Phys.* 95, 8011–8018 (2004).
117. D. M. Sullivan, and D. S. Citrin, "Determining quantum eigenfunctions in three-dimensional nanoscale structures," *J. Appl. Phys.* 97, 104305 (2005).
118. W. C. Chew, J. M. Jin, and E. Michielssen, "Complex coordinate stretching as a generalized absorbing boundary condition," *Microw. Opt. Technol. Lett.* 15, 363–369 (1997).
119. D. M. Sullivan, and P. M. Wilson, "Time-domain determination of transmission in quantum nanostructures," *J. Appl. Phys.* 112, 064325 (2012).
120. J. Shen, W. E. I. Sha, Z. X. Huang, M. S. Chen, and X. L. Wu, "High-order symplectic FDTD scheme for solving a time-dependent Schrödinger equation," *Comput. Phys. Commun.* 184, 480–492 (2013).
121. S. Datta, *Quantum Transport: Atom to Transistor*. New York: Cambridge University Press, 2005.
122. Y. S. Joe, A. M. Satanin, and C. S. Kim, "Classical analogy of Fano resonances," *Phys. Scr.* 74, 259–266 (2006).
123. M. Kauranen, and A. V. Zayats, "Nonlinear plasmonics," *Nat. Photonics* 6, 737–748 (2012).
124. J. J. Liu, M. Brio, Y. Zeng, A. R. Zakharian, W. Hoyer, S. W. Koch, and J. V. Moloney, "Generalization of the FDTD algorithm for simulations of hydrodynamic nonlinear Drude model," *J. Comput. Phys.* 229, 5921–5932 (2010).
125. W. E. I. Sha, W. C. H. Choy, and W. C. Chew, "The roles of metallic rectangular-grating and planar anodes in the photocarrier generation and transport of organic solar cells," *Appl. Phys. Lett.* 101, 223302 (2012).

126. W. E. I. Sha, W. C. H. Choy, Y. Wu, and W. C. Chew, "Optical and electrical study of organic solar cells with a 2D grating anode," *Opt. Express* 20, 2572–2580 (2012).
127. F. Z. Kong, W. Y. Yin, J. F. Mao, and Q. H. Liu, "Electro-thermo-mechanical characterizations of various wire bonding interconnects illuminated by an electromagnetic pulse," *IEEE Trans. Adv. Packag.* 33, 729–737 (2010).
128. A. Fang, T. Koschny, and C. M. Soukoulis, "Self-consistent calculations of loss-compensated fishnet metamaterials," *Phys. Rev. B* 82, 121102 (2010).
129. Z. X. Huang, T. Koschny, and C. M. Soukoulis, "Theory of Pump-Probe experiments of metallic metamaterials coupled to a gain medium," *Phys. Rev. Lett.* 108, 187402 (2012).
130. L. Pierantoni, D. Mencarelli, and T. Rozzi, "A new 3-D transmission line matrix scheme for the combined Schrodinger-Maxwell problem in the electronic/electromagnetic characterization of nanodevices," *IEEE Trans. Microw. Theory Tech.* 56, 654–662 (2008).
131. K. Lopata, and D. Neuhauser, "Multiscale Maxwell-Schrodinger modeling: A split field finite-difference time-domain approach to molecular nanopolaritonics," *J. Chem. Phys.* 130, 104707 (2009).